ACSNANO

www.acsnano.org

ARTICLE

Chiral Graphene Quantum Dots Enhanced Drug Loading into Small Extracellular Vesicles

Youwen Zhang, Gaeun Kim, Yini Zhu, Ceming Wang, Runyao Zhu, Xin Lu, Hsueh-Chia Chang,* and Yichun Wang*

Cite This: https://doi.org/10.1021/acsnano.3c00305

Read Online

ACCESS | Metrics & More | Article Recommendations | Supporting Information

ABSTRACT: **As nanoscale extracellular vesicles secreted by cells, small extracellular vesicles (sEVs) have enormous potential as safe and effective vehicles to deliver drugs into lesion locations. Despite promising advances with sEV-based drug delivery systems, there are still challenges to drug loading into sEVs, which hinder the clinical applications of sEVs. Herein, we report an exogenous drug-agnostic chiral graphene quantum dots (GQDs) sEV-loading platform, based on chirality matching with the sEV lipid bilayer. Both hydrophobic and hydrophilic chemical and biological drugs can be functionalized or adsorbed onto GQDs by $\pi-\pi$ stacking and van der Waals interactions. By tuning the ligands and GQD size to optimize its chirality, we demonstrate drug loading efficiency of 66.3% and 64.1% for doxorubicin and siRNA, which is significantly higher than other reported sEV loading techniques.**

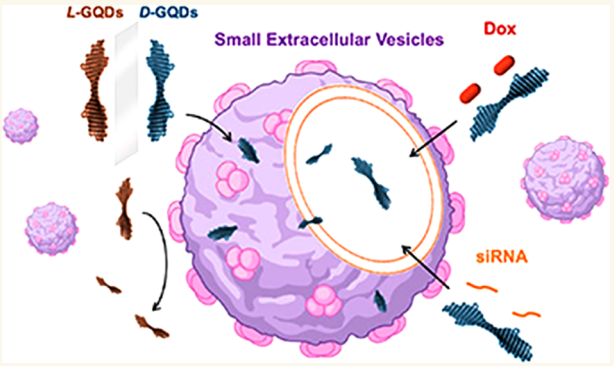

KEYWORDS: *chirality, extracellular vesicles, graphene quantum dots, chemotherapy, siRNA, drug delivery*

Extracellular vesicles (EVs) are a diverse group of vesicles that are enclosed by a membrane and actively secreted by nearly all types of cells. They are present in various human body fluids, such as blood, urine, saliva, and ascites. Small extracellular vesicles (sEVs), which refer to EVs with a diameter of less than 200 nm, are among the most extensively studied types of EVs due to their crucial roles in numerous physiological and pathological processes.[1] These vesicles are known to transport bioactive components, including nucleic acids and proteins, from donor cells to recipient cells, enabling intercellular communication. Recently, sEVs have been extensively explored as drug delivery vehicles due to their biological and functional characteristics such as low immunogenicity, long circulation time, nontoxicity, optimal biocompatibility, strong tissue penetration, enhanced targeting effect, and ability to cross the blood–brain barrier.[2] However, production and clinical applications of sEV-based drug delivery vehicles remain elusive due to drug loading challenges. sEV drug loading efficiencies of the available approaches are relatively low.[3,4] Most of these approaches potentially result in lipid damage, protein denaturation, and precipitation of nucleic acids.[5] Thus, efficient loading of various exogenous therapeutics into sEVs is gaining increasing recognition.[6]

Endogenous drug loading involves specific cell cultures or transfected/programmed cell cultures that secret drug-loaded sEVs.[3] It does not require any auxiliary loading apparatus and is hence quite simple. However, it cannot be used for chemical drugs, and the yield of secreted sEVs with biologics is generally low (<30%)[7] due to the myriad of intracellular sEV biogenesis and molecular sorting mechanisms. Active exogenous drug loading methods such as sonication, electroporation, extrusion, surfactant (saponin) permeabilization, liposome fusion, and freeze–thaw cycles aim to incorporate the drugs after sEV harvesting and isolation.[8] As these active methods involve disruption of the sEV bilayer, they can also lead to sEV lysis or fusion. Hence, the size distribution, function, zeta potential, and drug capacity of the cargo-loaded sEVs are sensitive to the loading procedures.[9] The most popular electroporation and sonication methods[10] can also damage the loaded cargos, leading to lipid degradation, protein denaturation, and nucleic acid precipitation due to acoustophoretic and electrophoretic effects and their related dipolar force fields at the single-molecule level.[11,12]

Received: January 10, 2023
Accepted: April 27, 2023

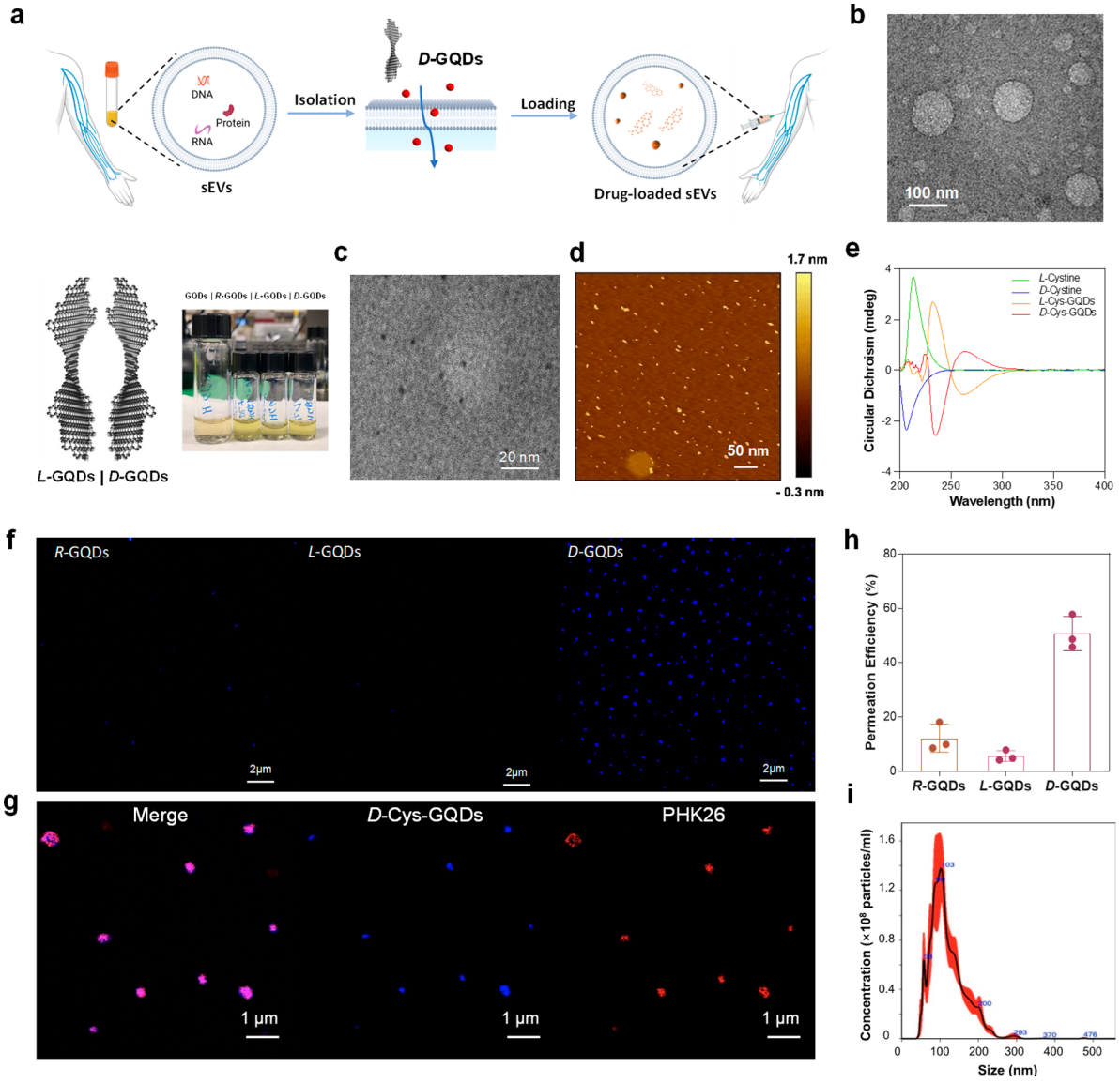

Figure 1. (a) The principle of chiral graphene quantum dots (GQDs)-enhanced drug loading into small extracellular vesicles (sEVs). (b) Transmission electron microscope (TEM) images of isolated sEVs by an asymmetric nanopore membrane (ANM). (c) Characterization of D-Cys-GQDs by transmission electron microscope (TEM), measured after 1 week of sample preparation, and TEM images of *R*-, *L*-, and D-Cys-GQDs are displayed in Figures S1a. (d) Atomic force microscopy (AFM) and (e) circular dichroism (CD). (f) Permeation of chiral GQDs (blue) into sEVs was evaluated by confocal microscope at room temperature. The samples were prepared by incubating 7.5 μM achiral or chiral GQDs with 3T3 sEVs (1.0×10^9 particles/mL) and then washing with PBS (4 °C) for four times under the support of a 100 kDa centrifuge tube. (g) Confocal images of PHK26-labeled sEVs (red) were taken after being treated with D-Cys-GQDs (blue). (h) Permeation efficiency was quantified by counts of GQD-loaded sEVs (blue) over the total counts of sEVs. (i) Size distribution and particle number of GQD-loaded sEVs were measured with nanoparticle tracking analysis (NTA).

Passive exogenous loading by incubation of drugs and extracted sEVs[13] is the least disruptive loading technology among the currently available methods. It is also the most scalable to large-volume production relevant to clinical translations and applications.[14] However, with just diffusion across the lipid bilayer as the only loading mechanism, passive incubation can only be applied to soluble drugs with lipophilic moieties.[15] Consequently, small interfering RNA (siRNA) cargoes are often conjugated with hydrophobic molecules to facilitate this transport. However, other than their potential toxic effects, such moieties often prevent luminal drug loading with the drug either adhering to the sEV or intercalated at its bilayer.[15,16] Without the conjugation of hydrophobic moieties, passive loading efficiency of soluble drugs is typically lower than 10%.[17,18]

Clearly, an easily optimized high-efficiency passive drug loading carrier that can adhere to the sEV bilayer but also permeate into the sEV luminal interior would be ideal. Due to their favorable hydrophobic and van der Waals interactions with lipid bilayer, graphene nanosheets have been suggested as a viable drug carrier that allows intercalation with the sEV lipid bilayer.[19] The delocalized electron of the graphene allows easy adsorption of hydrophobic drugs, and hydrophilic drugs can be functionalized directly onto the graphene. However, graphene drug carriers are often encapsulated within the bilayer without transit into the interior. In a recent study,[20,21] we discovered a potential mechanism that allows this final transit into the

https://doi.org/10.1021/acsnano.3c00305
ACS Nano XXXX, XXX, XXX−XXX

interior of the sEVs: chiral interaction between the graphene sheets and the lipid molecules.

As chirality is hard-wired into every biological system,[22] chirality of nanoparticles (NPs) plays a key role in their biomedical applications involving biological events, such as cell uptake, immune response, and tissue transport.[23] It was demonstrated that NPs coordinated with D-chirality displayed 3-fold higher permeability through cell membrane penetration in breast, cervical, and multiple myeloma cancer cells than those with L-chirality.[24] These D-formed NPs exhibited superior stability and longer biological half-lives *in vivo*.[25] Graphene quantum dots (GQDs), as single-layered graphene nanosheets, have widely been used in biomedical applications due to its low cytotoxicity and high biocompatibility,[26] optical properties,[27] and precisely controlled physical and chemical properties.[28] Most importantly, GQDs displayed superior passive transport properties[29] through cellular lipid membranes due to their two-dimensional (2D) morphology,[19] chemical structure,[30] and nanoscale dimensions.[26] In particular, GQDs with right-handed chirality (D-GQDs) derived from D-cystine[20] were previously reported to permeate phosphatidylcholine (POPC) lipid bilayers more efficiently compared to the ones with left-handed chirality (L-GQDs).[21] In addition, GQDs are capable of carrying a wide range of drugs with a high efficiency (>90%), and these drugs carried by GQDs with arbitrary charge can be hydrophobic or hydrophilic, biological or chemical via pi stacking and van der Waals interactions.[31,32] Therefore, a chiral GQD with right handedness is a potential tool to efficiently load drugs/genes into sEVs by passive transport through the sEV lipid bilayers that are similar to the membranes of the parent cells.[33,34]

In this work, we investigated the permeability of chiral GQDs into sEVs through a lipid membrane and their ability of passive drug loading in sEVs (Figure 1a). We found that D-GQDs derived from D-cysteine have a stronger tendency (52.4 ± 8.2% of permeation efficiency) to permeate into sEVs than pristine GQDs and L-GQDs, and the permeability of D-GQDs could further be improved to 85% after optimization. Taking advantage of chiral interactions between chiral NPs and biological lipid membranes, and the synergistic effect of the physical surface of chiral GQDs, we successfully loaded a hydrophobic chemotherapy drug—doxorubicin (Dox)—and a large biological drug—siRNAs—into sEVs. Dox/siRNA-loaded sEVs exhibited effective killing of cancer cells, with significant knock-down of the targeted gene and the inhibited expression of relative protein levels, respectively. Our work indicated that passive drug loading into sEVs enhanced by chiral GQDs is hence the most robust (drug-agnostic) and scalable loading method that requires minimal tuning. Therefore, our developed chiral GQD enhanced drug loading technology provides a promising platform for loading therapeutic sEVs for future clinical translation.

RESULTS AND DISCUSSION

Investigation of Chiral GQD Permeation into sEVs. To investigate the permeation efficiency of chiral GQDs into sEVs (Figure 1a,b), we first synthesized chiral GQDs derived by surface modification with L- and D-cysteine (L- and D-Cys-GQDs) using a previously reported method.[20] The structures of derived L- and D-Cys-GQDs were confirmed by the combination of spectroscopy and microscopy. Transmission electron microscope (TEM) images showed that L- and D-Cys-GQDs have a size distribution of 3.0−9.4 nm (Figure 1c and Figure S1a). Atomic force microscopy (AFM) images (Figure 1d) confirmed the size range of L- and D-Cys-GQDs in TEM. The thickness of L- and D-Cys-GQDs was within 2 nm, verified by AFM (Figure 1d), which corresponded to a single layer of chiral GQDs with enhanced height from helical buckling (twisting) of the pristine GQDs (~1 nm).[35,36] L- and D-Cys-GQDs showed positive and negative peaks at 236 nm, respectively (Figure 1e) in circular dichroism (CD) spectra. These chiroptical bands and *g*-factor (Figure S1b) of chiral GQDs showed opposite signs depending on the level of right- and left-handed twists of the 2D nanosheets, respectively, matching the chirality of L- and D-cysteine used for conjugation to the GQDs.[20] Cloud peaks at 264 nm indicated covalent bonding of cysteines on the edge of GQDs,[20] whereas the as-synthesized GQDs and *R*-Cys-GQDs (i.e., made with a racemic mixture of L- and D-cysteine) displayed no chiroptical activity in CD spectra (Figure S1c), either a high-energy peak at 220−250 nm or a low-energy peak at 250−300 nm. Furthermore, the UV−vis spectra (Figure S1d) of the chiral GQDs revealed two distinct absorption bands centered at 270 nm (ascribed to $\pi-\pi^*$ transitions in the sp^2-hybridized carbon core) and 375 nm (attributed to the $n-\pi^*$ transitions or carboxyl groups). It indicated partial relaxation of exciton confinement compared to pristine GQDs with a peak at 225 nm due to the hybridization of the aromatic system of GQDs with the atomic orbitals on cysteine moieties.[20] Being excited by photons with λ_{ex} = 360 nm, pristine GQDs showed emission at 480−540 nm, while L- and D-forms of GQDs displayed strong emission at 500−550 nm (Figure S1e). The red shift (~26 nm) after the modification with the amino acids in the photoluminescent (PL) peaks was caused by charge transfer between functional groups and the graphene carbon core of GQDs, which narrowed the band gap.[37,38] The zeta-potential (ζ) of as-synthesized GQDs was −21.8 ± 4.2 mV (Figure S1f). After attachment of cysteine moieties, ζ-potentials of L- and D-form chiral GQDs became −3.3 ± 2.1 mV and −1.6 ± 1.8 mV (Figure S1f), respectively. Such reduction of surface charge from GQD to L- and D-Cys-GQDs was consistent with amidation of negatively charged carboxyl groups (−COOH) at the edges of GQDs while retaining a substantial degree of ionization. Taken together, the combined results supported our successful synthesis of chiral GQDs.

Following the synthesis and characterization of L- and D-Cys-GQDs, we investigated the permeation of chiral Cys-GQDs into sEVs isolated from cell culture media of 3T3 cell lines (Figure 1b and Figure S2). As-synthesized GQDs and their chiral derivates (7.5 μM) were incubated with 3T3 sEVs (1.09×10^9 particles/mL) in phosphate-buffered saline (PBS) buffer (pH 7.4) at room temperature under a static condition. The permeation of GQDs and their chiral derivatives into sEVs was examined by confocal imaging based on the innate fluorescence of GQDs at 480−540 nm. sEVs after incubation with GQDs were washed with PBS buffer in a 100 kDa centrifuge tube until the fluorescence intensity of GQDs in the mixture decreased to a constant (Figure S3). The permeation of chiral GQDs into sEVs was detected by the accumulation of innate fluorescence of GQDs (around 525 nm, marked as blue) in the sEVs using a confocal microscope. Cys-GQDs with right-handed chirality (D-Cys-GQDs) showed a significantly higher density of blue dots (the accumulation of GQDs) than achiral *R*-Cys-GQDs and left-handed L-Cys-GQDs (Figure 1f) under the same concentration of the sEVs (10^8 particles/mL). To verify that the observed fluorescent signal of

https://doi.org/10.1021/acsnano.3c00305
ACS Nano XXXX, XXX, XXX−XXX

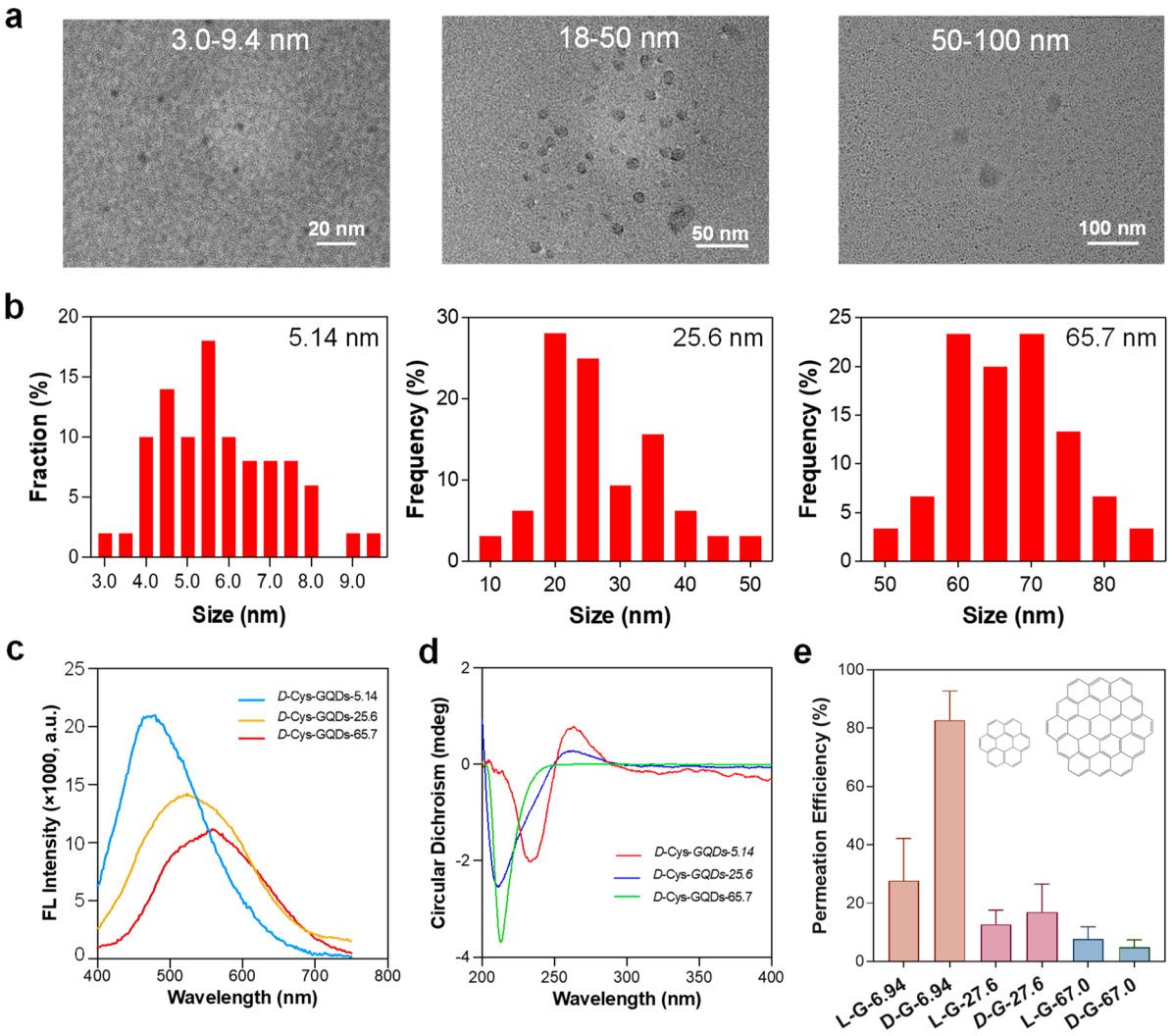

Figure 2. Size effect on permeation of chiral GQDs into sEVs. (a) TEM images and (b) histograms of size distribution of three size ranges of GQDs. Characterization of chiral GQDs under different size ranges, (c) fluorescent spectra excited at 360 nm, (d) CD spectra, and (e) permeation efficiency of size-dependent chiral GQDs (15 μM) into sEVs (10^9 particles/mL, L-G: L-Cys-GQDs and D-G: D-Cys-GQDs).

GQDs was inside sEVs, we labeled sEVs by staining their membranes using PKH26, which is a red fluorescent lipid membrane dye. The colocalization of PHK26-labeled sEV (red) and D-Cys-GQDs (blue) in Figure 1g demonstrated the permeation and accumulation of D-Cys-GQDs in the sEVs. To note, some point sources (100−500 nm) in the fluorescent image were about twice larger than the actual size of the objects (30−200 nm) due to the diffraction effects and resolution limitation of the optical microscope (180 nm laterally and 500 nm axially);[39] thus they were within the dimension range of sEVs. The permeation of chiral GQDs into sEVs was further quantified by fluorometry. The labeled EVs loaded with D-Cys-GQDs were lysed using 5 μL of RIPA (radioimmunoprecipitation) buffer. The change of the fluorescent intensity from the lysate was measured under the excitation wavelength of 365 nm (GQDs) and 550 nm (PHK26) (Figure S4a). The greatest fluorescent recovery (defined as the change in the emission fluorescence intensity before and after lysis for PHK26: 580 nm and GQDs: 510 nm) was achieved with D-Cys-GQDs, yielding a 3.6-fold increase of fluorescent intensity compared to L-Cys-GQDs and a 2.4-fold increase compared to *R*-Cys-GQDs, which provided further evidence for the highest permeation efficiency of D-Cys-GQDs.

In order to quantify the permeation efficiency of GQDs into sEVs, we developed a counting method based on image analysis (see Methods) to reflect the loaded sEVs at the single-sEV level. In short, the permeation efficiency of GQDs in sEVs was determined by statistically analyzing the total amount of GQD-loaded sEVs (blue dots larger than 30 nm as a threshold) over the total counts of sEVs from nanoparticle tracking analysis (NTA). D-Cys-GQDs exhibited significantly higher permeating efficiency (52.4 ± 8.2%) than *R*-Cys-GQDs (13.8 ± 4.7%), while L-Cys-GQDs (5.7 ± 2.2%) showed very limited permeation (Figure 1h). Most importantly, the size and morphology of sEVs retained integrity after the loading procedure by D-Cys-GQDs based on TEM and NTA results (Figure S4b and Figure 1i). This result aligned with the previous findings by molecular dynamics (MD) simulation that D-Cys-GQDs had a stronger tendency to penetrate the cellular lipid membrane of mammalian cells than L-Cys-GQDs.[20] This facilitated transport phenomenon is potentially attributed to the twist of 2D nanosheets that gives rise to nanoscale chirality with a single chiral center,[40] which, in turn, produces favorable interactions between chiral GQDs and the chiral lipid membrane of sEVs.

https://doi.org/10.1021/acsnano.3c00305
ACS Nano XXXX, XXX, XXX−XXX

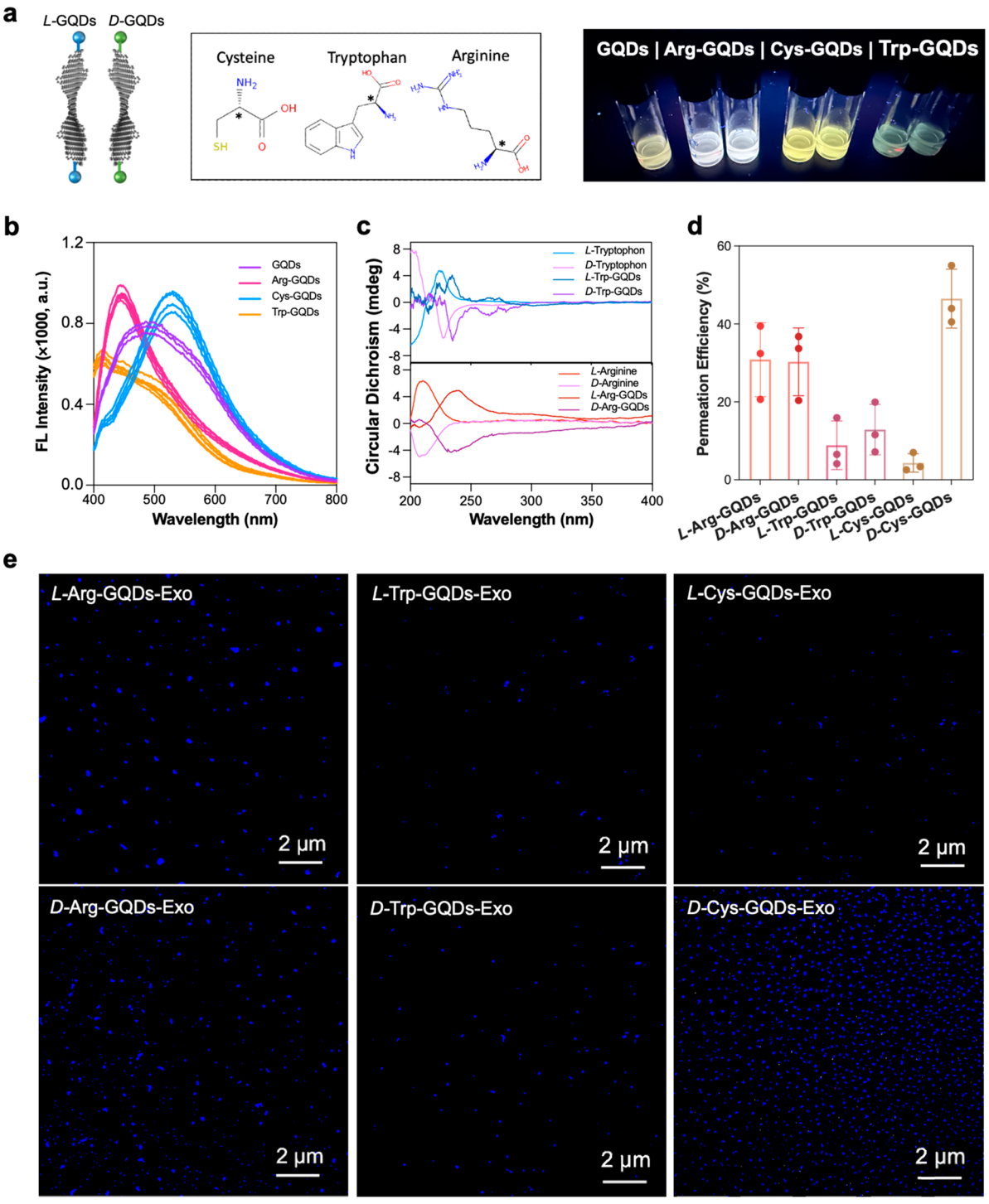

Figure 3. Effect of ligand on permeability of chiral GQDs into sEVs. (a) Photographs of the chiral GQDs depending on various ligands excited by UV light (λ_{max} = 365 nm). Characterization of GQDs and their chiral derivatives in (b) fluorescent spectra excited at 360 nm, (c) CD spectra and (d, e) permeation efficiency of chiral GQDs (7.5 μM) into sEVs (10^9 particles/mL) imaged by a confocal microscope at room temperature and quantified by analyzing images.

The Effect of Size on Permeability of Chiral GQDs into sEVs. The interaction of GQDs with the lipid bilayer membrane depends on the size of GQDs.[21] In particular, small GQDs (<13.3 nm) are able to enter the lipid bilayers with the membrane intact.[21,41] However, larger GQDs tend to deform the membrane with the formation of hemispherical vesicles and cause potential damage.[42,43] Moreover, the chirality originated by lattice distortion at the nanoscale is influenced by the size of NP lattices[44] and thus may affect the permeation efficiency of chiral GQDs in sEVs. Here, we investigated the effect of L- and D-Cys-GQDs (15 μM) with three different sizes on their permeation into sEVs (1.09×10^9 particles/mL). The average sizes of the three GQD samples were 5.14, 25.6, and 65.7 nm (Figure 2a,b) in this study. Due to the same tendency of fluorescence spectra and CD spectra (Figure S5a) of L- and D-Cys-GQDs, D-Cys-GQDs, which has higher permeation

https://doi.org/10.1021/acsnano.3c00305
ACS Nano XXXX, XXX, XXX−XXX

efficiency, is demonstrated in Figure 2 to show a size effect. With the size increase of chiral GQDs, a bathochromic shift was observed in fluorescent emission spectra of D-Cys-GQDs (excited at 360 nm, Figure 2c). The chirality corresponding to the nanoscale distortion was observed at a low-energy peak (250−300 nm) in CD spectra. Smaller D-Cys-GQDs (5.14 nm) exhibited higher chiroptical activities at 250−300 nm than the larger ones (25.6 and 65.7 nm). This was further confirmed by the CD peak at 265 nm of smaller D-Cys-GQDs associated with the Cotton effect (Figure 2d).[45] This phenomenon was potentially due to larger dihedral angles in the twisted molecular structures of the smaller chiral GQDs according to the previously reported study.[20] In addition, there were more terminal −COOH groups on larger GQDs, which increased the probability of anomalous and asymmetric bindings of cysteines, diminishing the symmetry-breaking perturbation of chiral edge ligands to electronic states of graphene nanostructures.[20,46] Following the characterizations of chiral Cys-GQDs with different sizes, we investigated the permeation of these L- and D-Cys-GQDs into sEVs isolated from 3T3 cell culture media by an ultracentrifugation method. The largest chiral GQDs (65.7 nm) showed limited permeation into sEVs according to the quantification method of permeation efficiency in the previous section (Figure 2e). This most likely occurs because the size of the largest GQDs (65.7 nm) was comparable to the size of sEVs (116 nm, Figure S1). Instead of passive transport through the membrane, the large GQDs damaged the lipid membranes of sEVs, confirmed by TEM images of sEVs (debris of sEVs observed in Figure S5b). Compared to the smaller D-Cys-GQDs (5.14 nm) with a permeation efficiency of 82.7% into sEVs, the ones with a median size (25.6 nm) had a low permeation efficiency (16.9%). This is consistent with the size distribution of the median GQDs, of which 9.4% are below 13.3 nm. The permeation efficiency of D-Cys-GQDs was 1.5 to 3 times higher than that of L-Cys-GQDs for both sizes of 5.14 and 25.6 nm, indicating the chirality-selective passive diffusion of GQDs through sEV membranes. Overall, the results suggested that small D-Cys-GQDs can permeate 3T3 sEV membranes most efficiently, which can be attributed to the relative size of GQD to sEV membrane thickness[42,43] and size-associated chirality generated from distortion of NP lattices.[44,47,48]

The Effect of Ligand on Permeability of Chiral GQDs into sEVs. According to our previous study,[20] the chirality of GQDs can be tuned by ligand types. This is because chiral ligands with different molecular weight, structures, and charges can change the dihedral angles of physical twists of nanosheets and thus generate different chirality at the nanoscale. Here, we use two alternative ligands, tryptophan and arginine, mainly because (1) tryptophan is a heavier chiral molecule than cysteine, which may result in a larger dihedral angle of nanosheet twist. Moreover, due to the benzene ring in tryptophan, there are multiple chiral centers generated by this ligand, which increases the complexity of chirality from chiral GQDs; (2) on the other hand, arginine, as a positively charged chiral molecule at pH 7, results in a smaller dihedral angle than cysteine due to its electrostatic interactions with carboxyl groups of GQDs, thus having lower chirality at the nanoscale. To investigate the ligand effect on permeation efficiencies of chiral GQDs into sEVs, GQDs were functionalized with another two chiral amino acids, arginine and tryptophan, by the same coupling reaction for L- and D-Cys-GQDs to generate different chiral GQDs (Figure 3a). The successful conjugations of arginine and tryptophan onto the edge of GQDs were supported by UV−vis absorption and fluorescent spectra. Both L-, D-Arg-GQDs and L-, D-Trp-GQDs had UV−vis absorption peaks at around 270 and 375 nm, which is similar to Cys-GQDs (Figure S6a). When excited at 360 nm, L/D-Arg-GQDs displayed strong emission at 400−500 nm (Figure 3b). A blue shift (∼40 nm) was observed compared to as-synthesized GQDs in the PL peaks due to the coupling of an electron-donating side chain that played a role of chromophore on GQDs. L- and D-Trp-GQDs showed a broad range of fluorescent emission compared to Cys-GQDs and Arg-GQDs with relatively lower intensity under the same concentration (7.5 μM). This was attributed to the fact that conjugating the large indole group of tryptophan to GQDs weakened the optical property (lower intensity of emission),[49] and increasing the size of GQDs changed the band gaps.[50] The chirality of these functionalized GQDs was determined and analyzed by CD spectra. CD spectra of both L-, D-Arg-GQDs and L-, D-Trp-CQDs gave rise to a symmetrical CD signal at around 240−300 nm. These peaks were different from those of free arginine and tryptophan near 220 nm, indicating the successful synthesis of chiral GQDs with chiroptical activity (Figure 3c,d). The zeta potentials (ζ) of chiral Arg-GQDs were +0.5 mV (L) and +0.3 mV (D), and those of Trp-GQDs were −1.1 mV (L), −0.7 mV (D) (Figure S6b).

We investigated the permeation of chiral GQDs derived from different chiral ligands (7.5 μM) into sEVs (10^9 particles/mL) under the same condition as in the previous section. D-Trp-GQDs reflected slightly higher permeation efficiency (15.63 ± 4.39%) into sEVs than L-Trp-GQDs (9.79 ± 6.48%). However, Trp-GQDs showed a significant reduction of permeation efficiency into sEVs compared with D-Cys-GQDs (Figure 2d,e). The potential reason is that the tryptophan with a large aromatic molecular structure (Figure 3a) gave rise to multiple chiral centers[51] and increased the complicity of chiral interactions of chiral GQDs with lipid bilayers of sEVs. Meanwhile, Arg-GQDs presented higher permeation efficiency (L, 31%; D, 29%) (Figure 3e) than Trp-GQDs; however, there is no selectivity between L- and D-Arg-GQDs. From the CD spectra, the lack of Cotton effect indicated that the chirality from Arg-GQDs originated from the surface enhancement of arginine attached on GQDs noncovalently. This also reflected on the broaden bands between 275 and 370 nm without cloud peaks with opposite signs of ligand chirality.[52] This is caused by the partial physical electrostatic absorption of the arginine ligand on the GQDs due to the charge of amino acids (+) and as-synthesized GQDs (−). These effects further implicated that nanoscale chirality originating from the twisting of a 2D nanosheet enhances the permeability of the biological lipid membrane through selective chiral interactions. Therefore, with the highest permeation efficiency due to the nanoscale chirality,[53] D-Cys-GQDs were chosen as the optimum chiral carriers for drug loading into sEVs in all the subsequent drug loading experiments.

The Effect of Concentration on Permeability of Chiral GQDs into sEVs. The concentration gradient of NPs across the lipid membrane is one of the main driving forces for NP transport through a lipid membrane.[54] Therefore, to optimize the permeation efficiency of chiral GQDs as a drug loading vehicle, we investigated the permeation efficiency of D-Cys-GQDs at different concentrations in the range of 0.75−30 μM in PBS buffer. With an increase in the concentration of the D-Cys-GQDs, a larger amount of D-Cys-GQDs entered the sEVs,

https://doi.org/10.1021/acsnano.3c00305
ACS Nano XXXX, XXX, XXX−XXX

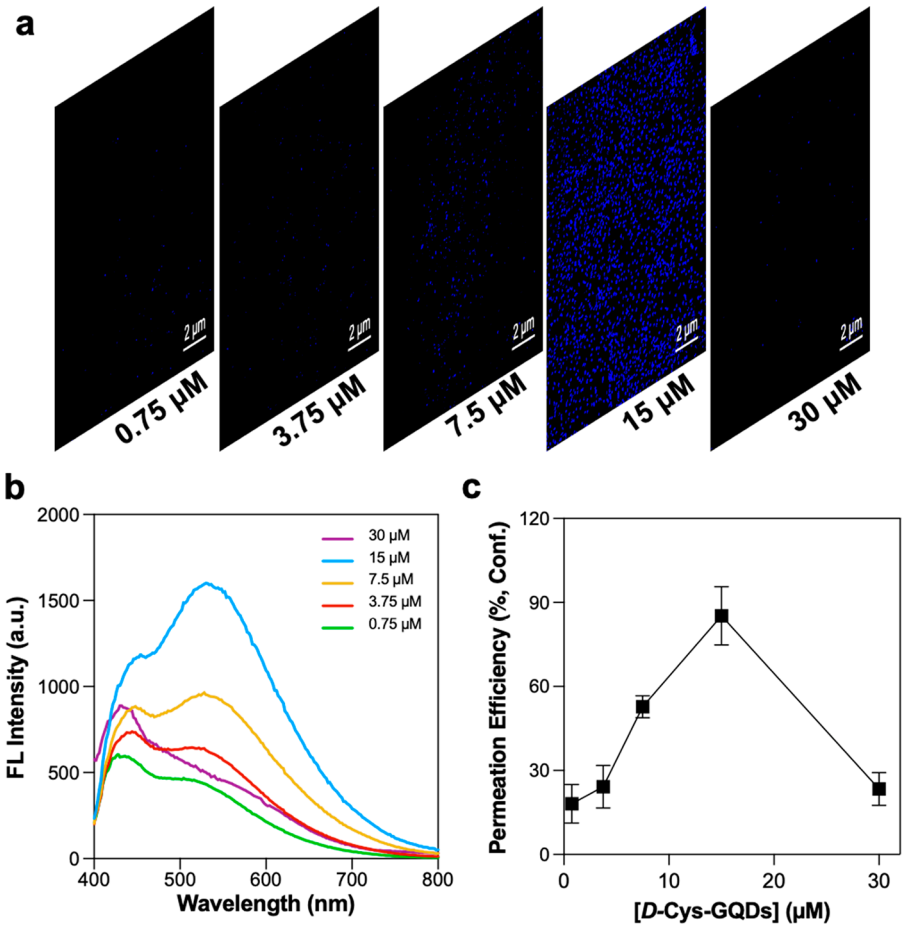

Figure 4. Effect of chiral GQD concentrations on their permeation into sEVs. (a) Confocal images of sEVs that were incubated with different concentrations of D-Cys-GQDs and then washed with PBS (4 °C) for four times under the support of a 100 kDa centrifuge tube. (b) Fluorescent spectra of D-Cys-GQDs-loaded sEVs excited at 360 nm and (c) statistical analysis of permeation efficiency of D-Cys-GQDs into sEVs.

indicated by more accumulation of D-Cys-GQDs (blue dots, Figure 4a) and higher retention fluorescent intensity of D-Cys-GQDs-loaded sEV solution (Figure 4b). Permeation efficiency of D-Cys-GQDs into sEVs was enhanced with the increased concentration in the range of 0.75 to 15 μM. However, the permeation efficiency of D-Cys-GQDs dropped significantly when the concentration of D-Cys-GQDs reached up to 30 μM (Figure 4b). This is potentially attributed to saturation of D-Cys-GQDs within the sEVs that eventually resulted in damage of sEVs at an external D-Cys-GQDs saturation concentration of 30 μM (Figure S7a). Overall, the highest permeation efficiency, 85.2 ± 10.3% of D-Cys-GQDs, into sEVs was achieved at a concentration of 15 μM (Figure 4c). All the subsequent drug loading experiments into sEVs were conducted at this optimized concentration of D-Cys-GQDs.

D-Cys-GQDs-Enhanced Chemotherapy Drug Loading into sEVs. After optimizing the permeability of chiral GQDs into sEVs, we evaluated the loading efficiency of a common hydrophobic chemotherapy drug, doxorubicin, facilitated by D-Cys-GQDs. Dox-loaded sEVs as a promising nanomedicine have shown enhanced therapeutic effects compared to the commercially available Dox-loaded liposomes.[55] However, loading Dox or other common drugs into sEVs remains challenging, which hinders their translational applications as drug delivery carriers.

D-Cys-GQDs can carry Dox molecules via $\pi-\pi$ stacking between the planar surface (carbon ring) of GQDs and the anthracene group of Dox molecules.[56] This binding can further be stabilized by electrostatic interaction between negatively charged surface functional groups, such as carboxylic groups, and the positively charged amino groups of Dox molecules.[57] (see Methods) Such D-Cys-GQDs/Dox complex can permeate the lipid bilayer of the sEV membrane with high efficiency, similar to the permeation efficiency of D-Cys-GQDs into sEVs (Figure 5a). The amount of Dox molecules carried by each D-Cys-GQD was determined by the quenching efficiency using the fluorescence resonance energy transfer (FRET) assay (Figure 5b).[58] As the concentration of D-Cys-GQDs increased, the quenching efficiency of Dox (200 μM) decreased dramatically. The quenching efficiency of Dox began to reach a plateau when concentrations of D-Cys-GQDs were higher than 15 μM (Figure S8a), which confirmed the attachment of Dox on the surface of D-Cys-GQDs. Based on the molar concentrations of Dox and D-Cys-GQDs at the plateau of quenching efficiency, each D-Cys-GQD was able to carry 14 Dox molecules (Figure S8b). The D-Cys-GQDs/Dox complex showed absorbance at both featured regions of D-Cys-GQDs and Dox, which further verified the attachment of Dox on the surface of D-Cys-GQDs (Figure S8c). Taken together, the combined results supported the formation of the D-Cys-GQDs/Dox complex.

https://doi.org/10.1021/acsnano.3c00305
ACS Nano XXXX, XXX, XXX−XXX

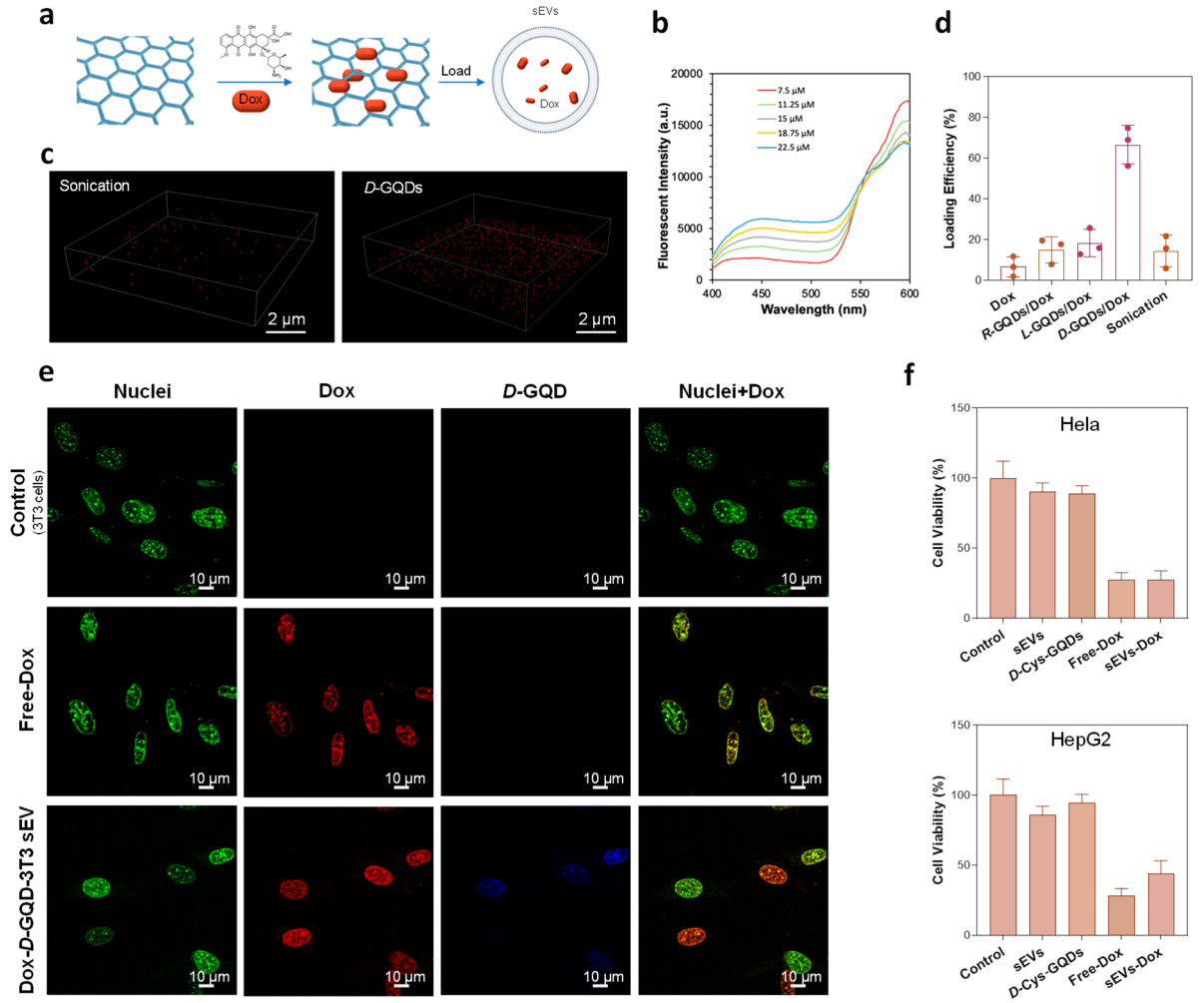

Figure 5. The chemotherapy drug doxorubicin (Dox) was loaded into sEVs by D-Cys-GQDs. (a) Schematic illustration of Dox loading into sEVs facilitated by D-Cys-GQDs. (b) Characterization of attachment of Dox (200 μM) directly onto the D-Cys-GQDs (7.5−22.5 μM) by fluorescent spectra (λ_{max} = 360 nm) and quenching efficiency. (c) Comparison of D-Cys-GQDs (15 μM) and sonication loading strategies for Dox (200 μM for both strategies) by a confocal microscope at room temperature. (d) Loading efficiency of Dox into sEVs facilitated by chiral GQDs. (e) Confocal images of free Dox and sEVs-Dox (loaded at a ratio of D-Cys-GQDs/Dox 15 μM/200 μM) uptake by 3T3 cells *in vitro* (scale bars: 10 μm) and (f) cell viability assessed using the CCK-8 assay.

We investigated the loading efficiency of the D-Cys-GQDs/Dox complex into sEVs at the optimized D-Cys-GQD concentration of 15 μM. For all the drug loading tests, D-Cys-GQDs/Dox (15 μM/200 μM) complexes were incubated with 3T3 sEVs (1.0×10^9 particles/mL) at room temperature under a static condition. The incubated solution was then washed with 1× PBS buffer in a 100 kDa cellulose centrifugal filter for multiple times to remove excessive D-Cys-GQDs/Dox complex. The change of the fluorescence intensity of the incubated solution was monitored at each washing step. The intensity of fluorescence decreased as the washing steps increased (Figure S9a−d). The fluorescent intensity of D-Cys-GQDs/Dox-loaded sEVs decreased moderately and kept the retention rate of 30.5% (Figure S9e), indicating the strong interaction between D-Cys-GQDs/Dox and sEVs. In contrast, a relatively steep decrease and low retention rate were observed for sEVs loaded by L-Cys-GQDs/Dox (24.4%), *R*-Cys-GQDs/Dox (21.9%), and free-Dox (11.5%) and a sonication method[59] (17.5%) (Figure S8e).

Drug loading via chiral GQDs into sEVs was further examined by confocal fluorescence microscopy by visualizing the colocalization of chiral GQDs (blue), sEVs (membrane dye in green), and the Dox (red) (Figure S10a). Due to FRET effect, all blue signals corresponding to GQDs variants were quenched by the attachment of Dox and thus showed relatively low intensity of signal in the confocal images (Figure S10a). Thus, the permeation of chiral-GQDs/Dox complex results were analyzed using the Dox channel (red) (Figure 5c and Figure S10b). Based on the definition of the encapsulation efficiency in the liposome formulation,[60] the drug loading efficiency of sEVs is defined to be the percentage of active sEVs that successfully encapsulate drugs (see Methods). Similar to the permeation efficiency of D-Cys-GQDs into sEVs, the loading efficiency of D-Cys-GQDs/Dox into sEVs (66.7 ± 9.5%) was significantly higher than that of L-Cys-GQDs/Dox (18.3 ± 6.7%). Meanwhile, the loading efficiency of *R*-Cys-GQDs/Dox (15.2 ± 6.3%) is the lowest among all samples (Figure 5d). In addition, sEVs loaded with Dox via the traditional sonication approach were prepared as a control. The low loading efficiency of traditional sonication (14.5 ± 7.9%) was reflected by a relative low density of Dox signal (Red) on confocal fluorescence microscopy (Figure 5c). Most importantly, sEVs retained integrity without significant change in size after drug loading by D-Cys-GQDs. In contrast, the

https://doi.org/10.1021/acsnano.3c00305
ACS Nano XXXX, XXX, XXX−XXX

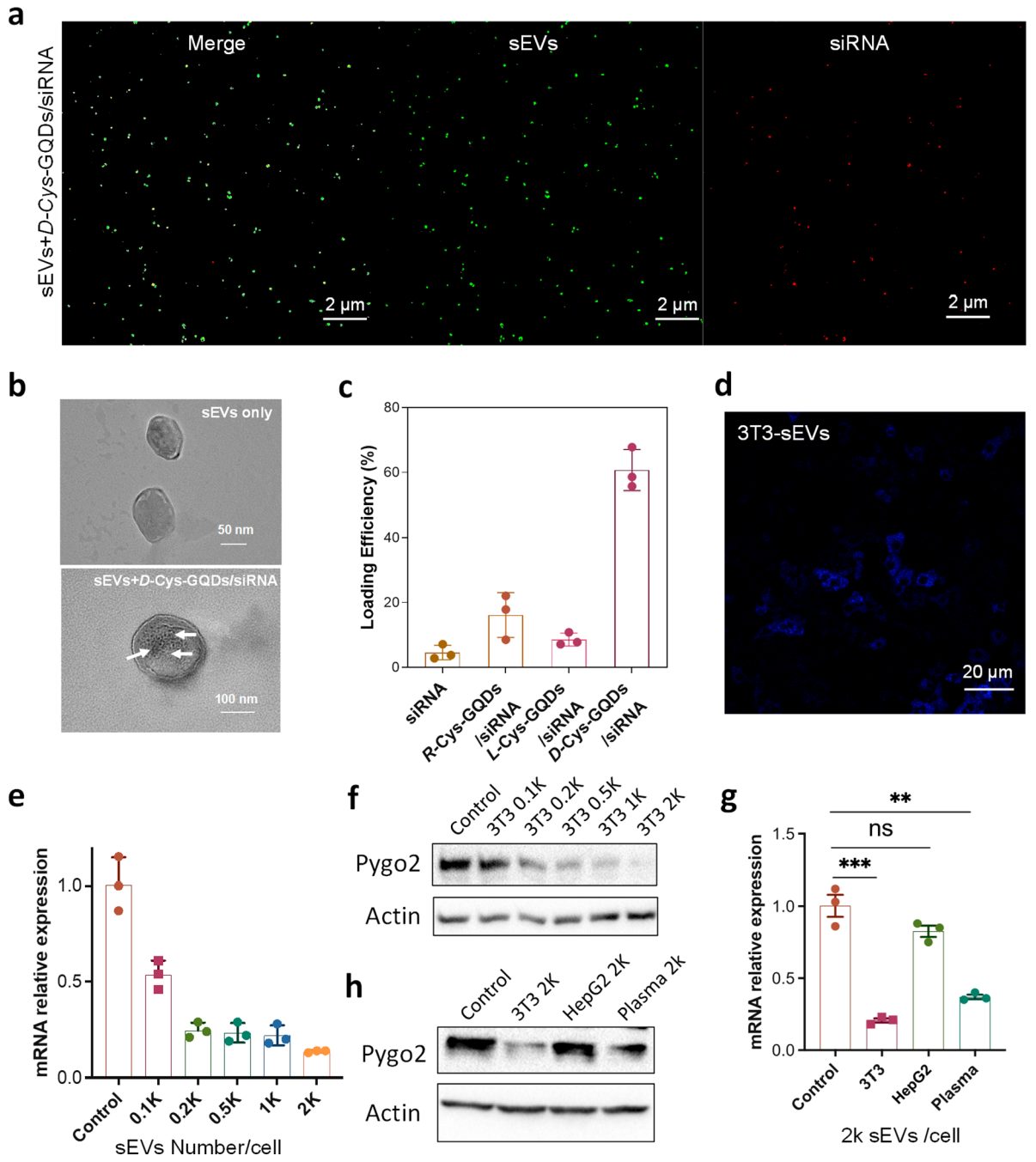

Figure 6. siRNA sEVs loaded by D-Cys-GQDs for gene therapy. (a) Confocal images of siRNA (red)-loaded sEVs (green) with facilitation of D-Cys-GQDs. (b) TEM demonstration of permeation of siRNA with the assistance of D-Cys-GQDs. (c) Loading efficiency of the chiral Cys-GQDs/siRNA complex into sEVs. (d) Confocal imaging of DU145 cell lines treated with 3T3 sEVs for 48 h (scale bars: 20 μm). (e, f) Pygo2 mRNA level (e) and protein level (f) in DU145 cells with the treatment of 3T3 sEVs loaded with D-Cys-GQDs/Pygo2 siRNA at different density for 48 h. (g, h) Comparison of Pygo2 silencing efficiency after being treated with D-Cys-GQDs/Pygo2 siRNA-loaded 3T3, HepG2, or plasma sEVs for 48 h through qPCR (g) and Western blot (h).

physical properties of sEVs were altered by sonication significantly, as shown in TEM and NTA (Figure S11a,b). These results demonstrated that drug loading into sEVs facilitated by chiral GQDs had significantly high efficiency and maintained the integrity of sEVs.

To evaluate whether D-Cys-GQDs/Dox-loaded sEVs (sEVs-Dox) can be taken up by the cells, we treated 3T3 cells with sEVs-Dox *in vitro* for 24 h and compared it to the control group treated with free Dox. The presence of Dox signals (red) in the confocal images demonstrated that Dox molecules were delivered successfully into the cells and mainly accumulated in the nucleus (Figure 5e); it is believed that doxorubicin exerts its effects via intercalation of DNA and the binding to proteins involved in DNA replication and transcription.[61] Meanwhile, D-Cys-GQDs (blue) were distributed mostly in the cytosol of cells, indicating the release of Dox from the D-Cys-GQDs/Dox complex, which hence does not require another drug release mechanism. These desirable properties make it possible to design concise and multifunctional drug delivery and release monitoring systems.[62]

https://doi.org/10.1021/acsnano.3c00305
ACS Nano XXXX, XXX, XXX−XXX

We then analyzed the ability of sEVs-Dox to inhibit cancer cell proliferation *in vitro*. Human hepatocellular carcinoma cells (HepG2) and cervical carcinoma cells (HeLa) were treated with sEVs-Dox for 24 h, while cells without treatment, those treated with control sEVs, and D-Cys-GQDs mixed with free Dox are negative controls. Cell viability of all samples was measured by the CCK-8 assay. sEVs-Dox inhibited cell proliferation by 44.2 ± 9.2% for HepG2 cells and by 27.4 ± 6.5% for HeLa cells, comparable to free Dox (HepG2: 28.3 ± 5.2% and HeLa: 27.7 ± 5.0%) (Figure 5f). Significant inhibition of cell growth was not observed in control samples treated with sEV and D-Cys-GQDs, indicating low or no toxicity associated with sEVs or D-Cys-GQDs. Dox-loaded sEVs by the sonication method were not included in the cell viability tests due to low yield of loaded sEVs that was caused by the damage of the physical structure of sEVs by sonication (Figure S11a,b).

Chiral GQD-Based siRNA Loading in sEVs for Gene Therapy. siRNA therapeutics are promising treatment for viral infections, hereditary disorders, and cancers.[63] However, it is still challenging in translational applications due to their poor intracellular uptake and the limited stability of siRNA in the bloodstream. When siRNA is administered intravenously, it is readily digested by nucleases and largely cleared from the kidney glomeruli before reaching the diseased organs. sEVs have been invested as nanocarriers for siRNA encapsulation to overcome this challenge due to the high stability in circulation[64] and efficient cellular uptake[65] compared with liposomes. However, the efficacy of siRNA loading in the sEV is relatively low,[8] as these nucleotides are relatively large and cannot diffuse into the sEV spontaneously.[66] Moreover, current methods, such as the usage of transfection reagents and viral transduction-based strategies, may affect the function of sEVs, and the pathogenicity and teratogenicity of the viruses may be preserved and inherited in sEVs, resulting in safety risks.[67,68]

Similar to enhanced Dox loading into sEVs through D-Cys-GQDs, we utilized D-Cys-GQDs to load the siRNA into 3T3 sEVs. The aromatic surface of GQDs can immobilize genomic substance drugs by $\pi-\pi$ stacking.[69] To demonstrate siRNA loading, a nucleic acid sequence (GUGCAAUGA-GGGACCAGUA) labeled with red dye ROX (carboxy-X-rhodamine) was tested first. The density of the siRNA on the D-Cys-GQDs surface was determined to be siRNAs per GQD by the same FRET assay (Figure S12) as the method for Dox. The optimized condition for loading was the chiral-Cys-GQDs/siRNA complex (15 μM/30 μM) determined by the saturation point of siRNA attachment on D-Cys-GQDs for the following loading investigation. The loading of D-Cys-GQDs/siRNA in sEVs was confirmed with confocal fluorescence microscopy by the colocalization signals of the labeled siRNA (red) and sEV (green, Cellmask green plasma membrane stain) (Figure 6a). Furthermore, we visualized D-Cys-GQDs/siRNA complex-loaded sEVs through TEM to confirm the successful loading. TEM images showed colocalization of D-Cys-GQDs/siRNA and sEVs with black dots in sight of individual sEVs compared with the bare ones (Figure 6b). The loading efficiencies were analyzed using the same method as in previous sections based on the red signal of siRNA (Figure S13a). Compared with free siRNA, which rarely entered sEVs, the loading efficiencies of D-Cys-GQDs/siRNA, *R*-Cys-GQDs/siRNA, and L-Cys-GQDs/siRNA were 64.1 ± 16.5%, 17.8 ± 7.4%, and 7.1 ± 4.2% (Figure 6c and Figure S13a). In addition, the size of siRNA-loaded sEVs remained similar to unloaded sEVs shown in NTA (Figure S13b). The results demonstrated that siRNAs were successfully loaded in the sEVs by chiral GQDs, and the sEVs retained integrity after the loading procedure.

To determine whether siRNA-loaded sEVs by D-Cys-GQDs are effective and efficient for cancer treatment, we chose a recently identified oncogene Pygo2 in prostate cancer as a target. Pygo2 is a chromatin effector and has been reported to have overexpression in prostate, ovarian, breast, cervical, hepatic, lung, intestinal, and brain cancers.[70] We recently also found that Pygo2 played an essential role in immunosuppressive tumor microenvironment regulation and inducing the resistance of prostate cancer to immunotherapy.[71] Therefore, targeting Pygo2 has very good implications in clinical treatment for many types of cancer. We have demonstrated the gene knock-down using commercially available Pygo2 (Pygopus homologue 2) siRNA. Pygo2 has good efficiency on silencing and has been used for gene delivery application.[72] Meanwhile, DU145 is a widely used human prostate cancer cell line with a high expression of Pygo2. Thus, we assessed D-Cys-GQDs/siRNA-loaded sEVs using a DU145 cell culture *in vitro*. First, we tested the uptake of the isolated 3T3 sEVs by the DU145 cell line. A strong fluorescent signal (blue: GQDs) was observed in the cytoplasm of DU145 cells incubated with D-Cys-GQDs-loaded (3T3) sEVs for 48 h (Figure 6d). Efficiencies of gene knock-down by D-Cys-GQDs/siRNA-loaded sEVs were confirmed with qRT-PCR and Western blotting. For 3T3 sEVs (100 to 2000 sEVs/cell), it showed significant reduction of Pygo2 mRNA levels by 45−80% with a mean value of 62% (Figure 6e). The expression of Pygo2 protein levels in DU145 cells was also silenced by D-Cys-GQDs/siRNA-loaded (3T3) sEVs by 22−91%, compared to the control group (Figure 6f). In addition, D-Cys-GQDs/siRNA induced a dose-dependent decrease for both mRNA and protein expressions. To reflect loading reliability of D-Cys-GQDs, sEVs isolated from two other sources, HepG2 cell culture medium and healthy human plasma, were tested as controls. Similarly, D-Cys-GQDs/siRNA-loaded plasma sEVs reduced expression of mRNA by 63.3 ± 7.8% (Figure 6g) and expression of protein by 50% (Figure 6h). HepG2 sEVs showed no obvious reduction of mRNA and Pygo2 protein, which contributed to the fact that the sEV uptake capabilities were different depending on the recipient cell types.[73] An overall 60−80% knock-down of the target gene and higher than 60% inhibition of Pygo2 protein indicated the efficacy of D-Cys-GQDs/siRNA-loaded sEVs to the target cells. Overall, D-Cys-GQDs can facilitate loading genes such as siRNA into sEVs without membrane damage of sEVs, and the loaded sEVs can successfully mediate silencing of target genes with high efficiency.

To compare our loading strategy with the other known method in terms of cytotoxicity and RNA stability, we loaded siRNA into sEVs by D-Cys-GQDs and a common transfection reagent, Lipofectamine 2000 (Lipo-2000). First, we tested cytotoxicity of siRNA-loaded sEVs on HepG2 cells. HepG2 cells were incubated with siRNA-loaded sEVs (10 000 particles/cell) for 24 h. The responses of cells to siRNA-loaded sEVs were monitored by CCK-8 assay (Figure S14a). siRNA-loaded 3T3-sEVs by D-Cys-GQDs exhibited no inhibition of cell proliferation (cell viability: >95%), while siRNA-loaded 3T3-sEVs by Lipo-2000 presented slightly higher toxicity in HepG2 cells (cell viability: 76%), which

https://doi.org/10.1021/acsnano.3c00305
ACS Nano XXXX, XXX, XXX−XXX

can potentially be attributed to the fusion of cationic lipids with sEVs. Moreover, confocal fluorescent images of the sEV solution (Figure S14b) after transfection of a ROX-labeled siRNA by Lipo-2000 suggested that the siRNA and Lipo-2000 formed large aggregates that were not able to fuse to the sEV membrane or enter the sEVs. In contrast, chiral-GQD-assisted siRNA loading strategy produced excellent dispersion after the loading and the sEVs retained integrity after siRNA loading by D-Cys-GQDs (Figure S14c). In addition, we tested controls, including 3T3-sEVs (10 000 particles/cell), Lipo-2000 (1 μL, unknown concentration, Thermo Fisher Scientific), Lipo-2000/siRNA (1 μL/20 pmol), D-Cys-GQDs (15 nM), and D-Cys-GQDs/siRNA (15 nM/30 nM). Bare 3T3-sEVs displayed no cytotoxicity toward HepG2 cells. Meanwhile, inhibition of cell growth was not observed in the control samples treated with D-Cys-GQDs and D-Cys-GQDs/siRNA, indicating low or no toxicity associated with D-Cys-GQDs and their complex D-Cys-GQDs/siRNA. Lipo-2000 and Lipo-2000-encapsulated siRNA showed a slight toxicity in HepG2 cells (cell viability: 60−70%), which is due to the side effect of cationic lipid on caspase activation dependent signaling pathway and mitochondrial dysfunction.[74] siRNA stability was evaluated by the Bioanalyzer system (Figure S14d), which is a tool commonly used to assess the quality of RNA samples. It uses microfluidic electrophoresis to separate RNA molecules based on size and generate a digital electropherogram that provides valuable information on the quality of RNA samples before downstream applications.[75] The siRNA loading strategies using chiral GQD exhibited a consistent size distribution of siRNA (Pygo2) that is comparable to the siRNA control group, as well as the traditional transfection reagent. Overall, the chiral-GQD-assisted loading strategy exhibited lower cell toxicity and similar RNA stability than the common transfection agent loading method.

CONCLUSION

In summary, we have developed an exogenous drug-agnostic chiral GQDs sEV-loaded platform, based on chirality matching with the sEV lipid bilayer. Both hydrophobic and hydrophilic chemical and biological drugs can be functionalized or adsorbed onto GQDs by π−π stacking and van der Waals interactions. By tuning the ligands and GQD size to optimize its chirality, we demonstrate significantly higher drug loading efficiency for Dox and siRNA into sEVs by D-Cys-GQDs at an optimal concentration, compared to other reported sEV loading techniques.[15] The drug-loaded sEVs by D-Cys-GQDs are shown to be effective in killing cancer cells, the knockdown of the target gene, and the inhibition of mRNA and relative protein expression levels. Thus, chiral-GQD-enhanced drug loading is a promising generic and scalable drug loading technique that can enable high-throughput production of therapeutic sEVs for clinical applications.

METHODS AND EXPERIMENTAL SECTION

Isolation and Characterization of sEVs. The Hep-G2 and 3T3 cells were purchased from the American Type Culture Collection (ATCC) and propagated in minimum essential medium (MEM, Corning Incorporated, Corning, NY, USA) supplemented with 10% fetal bovine serum (FBS) (sEV-depleted) and antibiotics. All cells were maintained in 5% CO_2 at 37 °C, and the cell culture medium (CM) was collected for 24 h. Then, the CM was centrifuged at 500*g* for 10 min, 2000*g* for 10 min, and 12000*g* for 30 min to remove cells and cell debris. The supernatants were pelleted by ultracentrifugation at 100000*g* for 80 min. However, we found the yield of ultracentrifugation to be too low to produce sufficient sEVs for loading, to the extent that pellets were not found for some cell media samples. Instead, we adopted an ultrafiltration method based on our earlier work. The nanopores of ion-track membranes are etched into conic pores[76] to allow high-throughput isolation, enrichment, and purification with minimum loss of the sEVs.[77,78] The data reported are mostly from this asymmetric nanopore membrane (ANM) ultrafiltration technique (Aopia Biosciences, USA) with a flow rate of 20 mL/h. A typical NTA characterization of ANM-filtered sEVs is seen in Figure S1b in the Supporting Information. sEVs were dissolved with PBS buffer and stored at −80 °C until use.

sEV markers CD63 [1:1000; Cell Signaling Technology (CST), USA] and Alix (1:1000; Abcam, UK) and the ER marker calnexin (1:1000; Abcam, UK) were detected by Western blotting. The size distribution and zeta potential of N-Ex were measured by the NanoSight LM10 system (NTA, UK). The PDI of N-Ex was tested by dynamic light scattering (DLS, Malvern Instruments, UK).

Nanoparticle tracking analysis measurements were performed with a NanoSight NS300 (NanoSight Ltd., UK) using purified sEVs (100 μL in 1 mL of PBS buffer). The mean sEV size distribution (modal hydrodynamic diameter in nm) and sEV concentration (number of EVs enriched from 1 mL of sample in particles/mL) were captured and analyzed with the NTA 3.3 analytical software suite. All procedures were performed at room temperature.

The morphology of sEVs was identified by TEM (JEOL 2011) and AFM (Park XE7, Korea). Its structure was further characterized by electron microscopy (EM). Purified sEVs were resuspended in PBS and fixed with 2% paraformaldehyde for 30 min at room temperature. Eight microliters of mixture was then dropped onto EM grids that had been pretreated with UV light to reduce static electricity. After drying for 30 min, sEVs were stained twice (6 min each) with 1% uranyl acetate. The dried grids were examined using an HT7700 (JEOL 2011) transmission electron microscope at 120 kV.

GQD and Chiral GQD Synthesis. The carbon nanofibers (100 nm), L- and D-cysteine, sulfuric acid, nitric acid, *N*-(3-(dimethylamino)propyl)-*N*′-ethylcarbodiimide hydrochloride (EDC, 191.7 g/mol), and *N*-hydroxysulfosuccinimide sodium salt (Sulfo-NHS, 217.13 g/mol) were purchased from Sigma-Aldrich. The GQDs were synthesized by a modified protocol from our previous report.[20,79] Briefly, 0.4 g of carbon nanofibers was dispersed into a 40 mL mixture of sulfuric acid and nitric acid (3:1, v/v) and sonicated for 2 h. The mixture was mechanically stirred for 6 h at room temperature followed by being heated to 120 °C to continuously react for 10 h. After the reaction, the mixture solution was cooled and diluted with ice DI water, and the pH adjusted to 8 by adding sodium hydroxide. Then, the GQDs was purified with 3 days' dialysis, and the final concentration of GQDs was 1 mg/mL. In order to impart chirality to the GQDs, the carboxylic group of GQDs was connected with the amine group of L-(or D-)cysteine by the EDC/NHS method.[58,80] Briefly, a solution of EDC (20 μL, 100 mM) was added into 2 mL of GQD (100 μM) solution. After 10 min of stirring, 40 μL of Sulfo-NHS (100 mM) was added to the solution, and it was sonicated for 40 min under an ice−water bath.[81] The resulting mixture was treated by a 1 kDa centrifuge tube and rinsed three times to remove excess EDC and Sulfo-NHS. Finally, 40 μL of L- (or D-) cysteine (100 mM) was added into the GQD-NHS ester, and the mixture was stirred for 2 h. The surplus L- and D-forms of cysteine were removed by a dialysis membrane (1 kDa, Fisher Scientific). The density of the cystine molecules on GQDs was determined to be 2.6 using a colorimetric-based assay[82] in Figure S15 and validating with the absorbance of chiral GQDs in Figure S1f at 375 nm. Relatively large size GQDs were obtained with average size tunable by reaction time.[83] After 2 h of reaction under the same condition (sulfuric acid and nitric acid were 3:1 in v/v), the size of GQDs was found to be around 3−90 nm (mean value: 50 nm). The solution was separated and cut off by using two sizes of nanoporous membrane (18 and 50 nm). The small-size GQDs (<18 nm) in this bench was discarded. The middle size (18−50 nm) and large size (50−90 nm) in this bench were collected, and then they were modified with L- and D-

https://doi.org/10.1021/acsnano.3c00305
ACS Nano XXXX, XXX, XXX−XXX

cysteine using the same EDC/NHS method. The size was characterized by TEM (Figure 2).

The chiroptical activity of the dispersions was measured by CD spectroscopy (J-1700, JASCO), and the chemical reaction progress was monitored by FT-IR spectroscopy (FT/IR-6300, Jasco) and Raman spectroscopy (NRS-5100, Jasco). The absorbance of chiral GQDs was analyzed by UV/vis spectroscopy (Agilent, 89090A). The fluorescence property of chiral GQDs was characterized by an Infinite M1000 plate reader (Tecan Group). The morphology of chiral GQDs was observed by TEM (JEOL 2011). Their surface potential was analyzed by a Zetasizer (Malvern Instruments, Nano ZS).

Cell Cultures and Viability Assays. 3T3 and hepatocellular carcinoma human cells (HepG2) (ATCC, VA) were maintained with Eagle's minimum essential medium (EMEM) supplemented with 10% FBS and 1% penicillin−streptomycin (ATCC) in a humidified incubator (MCO-15AC, Sanyo) at 37 °C in which the CO_2 level was maintained at 5% before seeding. All of the medium was filtered using a 0.22 μ SteriCup filter assembly (Millipore, USA) and stored at 4 °C for no longer than 2 weeks. For cells incubated with the siRNA-sEVs, and control sEVs, the cells were cultured overnight to allow attachment in a 96-well plate and confocal dishes, washed with FBS-free EMEM, and then incubated with sEV analytes at 37 °C for 1 h in FBS-free medium. After incubation with difference windows, the cells were washed repeatedly with sterilized PBS and maintained in culture medium before further analysis.

Cell viability was assessed using a Cell Counting Kit-8 (CCK-8 assay, Enzo). In brief, 3T3 and HepG2 cells were seeded into a 96-well flat culture plate (Corning). After being cultured overnight, the cells were washed with FBS-free EMEM and incubated with a specific concentration of sEV and sEVs in FBS-free medium at 37 °C for 12, 24, 36, and 48 h. The cells were then washed three times with sterilized PBS and incubated overnight with fresh medium containing 10% FBS. The cells were then washed with PBS and FBS-free EMEM (500 mL) before adding assay reagent. After incubation for 20 min at 37 °C, the cell proliferation and cytotoxicity were measured by absorbance at 460 nm. The background was measured by 3T3 and HepG2 cells cultured in FBS-free EMEM only.

Loading Therapeutic Cargo. To load the sEVs with Dox, 150 μL of purified sEVs and 50 μL of complex (40 μM D-Cys-GQDs: 560 μM Dox) were gently mixed at 4 °C, and the mixture was incubated at room temperature for 20 min to ensure the full permeation. To load the sEVs with siRNA, 150 μL of purified sEVs and 50 μL of complex (40 μM D-Cys-GQDs and 80 μM siRNA) were gently mixed at 4 °C, and the mixture was incubated at 37 °C for 20 min to ensure the full permeation. Recovery was assessed by analysis of confocal images as described above. sEVs were then washed with PBS (4 °C) four times under the support of a 100 kDa centrifuge tube to remove unincorporated free D-Cys-GQDs/siRNA. The sEVs loaded with siRNA were quantified for the encapsulated genomic drug by detecting the intrinsic fluorescence of labeled siRNA using the Infinite M1000 plate reader (Tecan Group) at 608 nm with excitation at 588 nm and image analysis of the confocal microscope under excitation at 561 nm.

Determination of the Permeation Efficiency of Chiral GQDs. The permeation efficiency of GQDs in sEVs was indirectly determined by statistically analyzing the count of blue-fluorescent lit-up sEVs (caused by permeation) under confocal microscopy over the total concentration of sEV after loading. In brief, 5 μL of loaded sEV sample was fully covered with 18 mm × 18 mm cover glasses (Corning, square, No. 1) and scanned under a 100× objective with a normal field size of 150 μm × 150 μm. Four Z-stacks of images were captured through random domains. Each Z-stack contained around 20−30 images from presenting to disappearing fluorescent dots with a step size of 0.125 μm. Then, captured images were analyzed using ImageJ. The total fluorescent sEV particles (TFEPs) were counted by settings with manually adjusted thresholds and matching the size of sEVs. Colocalized fluorescent sEV particles (CFEPs) of Z-stack images were counted based on centers of mass-particle coincidence by using the JACOPx Plugin. The permeation efficiency into sEVs was calculated using the following formula:

$$\text{Permeation efficiency (\%)} = \frac{\sum(\text{TFEPs} - \text{CFEPs})}{4 \times \text{TEPs}} \times \frac{18\ \text{mm} \times 18\ \text{mm}}{150\ \mu\text{m} \times 150\ \mu\text{m}} \times \frac{1}{5\ \mu\text{L}} \times 100$$

where TECs is the total sEV concentration (particles/mL) that is measured by NTA.

Determination of Loading Efficiency of Drug in sEVs. While the success of the drug loading procedure was mostly reported in the form of loading efficiency (the percentage of total available drug that has been encapsulated within EVs) or loading capacity (the amount of drug loaded per mass of particles),[84] it is only applicable for reflecting the concentration of active drugs and cannot realistically be applied for defining reproducible protocols of the exogenous loading of sEVs.[15] By taking the encapsulation efficiency of the liposome formulation,[60] loading efficiency for sEVs, which measures the percentage of active sEVs that successfully encapsulate drugs, was used in the design of sEV-based drug delivery systems. The same as the GQDs' permeation, the loading efficiency of Dox and siRNA in sEVs was indirectly determined by statistically analyzing the count of red fluorescent lit-up sEVs (caused by loading) under confocal microscopy over the total concentration of sEVs after loading. The loading efficiency into sEVs was calculated using the following formula:

$$\text{Loading efficiency (\%)} = \frac{\sum(\text{TFEPs} - \text{CFEPs})}{4 \times \text{TEPs}} \times \frac{18\ \text{mm} \times 18\ \text{mm}}{150\ \mu\text{m} \times 150\ \mu\text{m}} \times \frac{1}{5\ \mu\text{L}} \times 100$$

where TECs is the total sEV concentration (particles/mL) that is measured by NTA.

Western Blot. 3T3 cell derived sEVs were added to 1× RIPA buffer (Cell Signaling) to lysate, and samples were separated by SDS-PAGE. The separated proteins were transferred to a nitrocellulose membrane (Biorad) and treated with anti-CD9 antibody, anti-CD63 antibody, anti-CD81 antibody, anti-CD9 antibody (EXOAB-KIT-1, SBI), and anti-β-actin antibody (Santa Cruz Biotechnology). A secondary anti-rabbit antibody labeled with horseradish peroxidase (SBI) and anti-mouse HPR-linked antibody (Cell Signaling) were used, and immunoreactive species were detected by a Clarity Max Western ECL Substrate (Biorad).

Stability Test of siRNA. For conventional loading of siRNA into sEV, siRNA and chemical transfection reagent (Lipofectamine-2000, ThermoFisher) were mixed with a 2:1 ratio followed by incubation for 15 min at room temperature. Then an sEV suspension was added to the siRNA−Lipofectamine complex and incubated at 37 °C for 20 min. sEVs were then washed with PBS four times with the 100 kDa centrifuge tube to remove the free siRNA−Lipofectamine complex. A bioanalyzer (2100 Bioanalyzer System, Agilent) was used to measure the size of siRNA before and after loading into EVs.

ASSOCIATED CONTENT

Supporting Information

The Supporting Information is available free of charge at https://pubs.acs.org/doi/10.1021/acsnano.3c00305.

Figures S1−S15: Characterizations of 3T3 sEV, GQDs, and chiral GQDs; penetration studies of chiral GQDs on sEV; TEM images of sEVs treated with D-Cys-GQDs; confocal images of PHK26-labeled sEVs; UV−vis absorption and zeta potential of the L-/D-Arg-GQDs and L-/D-Trp-GQDs; the effect of D-Cys-GQD concentrations on the fluorescence intensity and the quenching efficiency of Dox; and the profile of siRNA-loaded sEVs (PDF)

https://doi.org/10.1021/acsnano.3c00305
ACS Nano XXXX, XXX, XXX−XXX

AUTHOR INFORMATION

Corresponding Authors

Hsueh-Chia Chang − *Department of Chemical and Biomolecular Engineering, University of Notre Dame, Notre Dame, Indiana 46556, United States;* orcid.org/0000-0003-2147-9260; Phone: 574-631-5697; Email: hchang@nd.edu; Fax: 574-631-5697

Yichun Wang − *Department of Chemical and Biomolecular Engineering, University of Notre Dame, Notre Dame, Indiana 46556, United States;* orcid.org/0000-0002-4353-6660; Phone: 574-631-2617; Email: ywang65@nd.edu; Fax: 574-631-2617

Authors

Youwen Zhang − *Department of Chemical and Biomolecular Engineering, University of Notre Dame, Notre Dame, Indiana 46556, United States;* orcid.org/0000-0001-8525-3418

Gaeun Kim − *Department of Chemical and Biomolecular Engineering, University of Notre Dame, Notre Dame, Indiana 46556, United States*

Yini Zhu − *Department of Biological Sciences and Integrated Biomedical Sciences Graduate Program, University of Notre Dame, Notre Dame, Indiana 46556, United States*

Ceming Wang − *Department of Chemical and Biomolecular Engineering, University of Notre Dame, Notre Dame, Indiana 46556, United States*

Runyao Zhu − *Department of Chemical and Biomolecular Engineering, University of Notre Dame, Notre Dame, Indiana 46556, United States*

Xin Lu − *Department of Biological Sciences, University of Notre Dame, Notre Dame, Indiana 46556, United States*

Complete contact information is available at: https://pubs.acs.org/10.1021/acsnano.3c00305

Author Contributions

Y.W. and Y.Z. conceptualized the study. Y.Z. designed and carried out the experiments. G.K. did biological and drug loading experiments, comparing the chiral GQD method for sEV loading with the sonication method, the transfection method, and isolated and characterized sEVs. Y.Z. did the *in vitro* test and quantified the protein expression and mRNA levels. C.W. isolated sEVs by ANM. R.Z. took the TEM images and assisted in the synthesis of chiral GQDs. H.C. and Y.W. supervised all the work, administrated the project, and acquired the funding. Y.Z. and Y.W. prepared the manuscript, and all authors contributed to data interpretation, discussions, and writing.

Notes

This paper has been previously submitted to a preprint server: Youwen Zhang, Yini Zhu, Gaeun Kim, Ceming Wang, Runyao Zhu, Xin Lu, Hsueh-Chia Chang, Yichun Wang. Chiral Graphene Quantum Dots Enhanced Drug Loading into Exosomes. 2023. bioRxiv. 2023.01.20.523510, 10.1101/2023.01.20.523510.

The authors declare no competing financial interest.

ACKNOWLEDGMENTS

This work was financially supported by American Cancer Society Institutional Research Grant (ACS IRG-17-182-04) at the Harper Cancer Research Institute, the National Science Foundation Industry-University Cooperative Research Center (The Center for Bioanalytic Metrology), and the National Institue of Health (NIH) Common Fund, through the Office of Strategic Coordination/Office of the NIH Director, 1UG3CA241684-01. The authors would like to thank J. Johnston for help with CD spectra and TEM images of chiral GQDs.

REFERENCES

(1) Jia, Y.; Li, Y.; Ma, T.; Xu, W.; Qian, H.; Sun, Y.; Shi, H. Small Extracellular Vesicles Isolation and Separation: Current Techniques, Pending Questions and Clinical Applications. *Theranostics.* **2022**, *12*, 6548−6575.

(2) Tenchov, R.; Sasso, J. M.; Wang, X.; Liaw, W.-S.; Chen, C.-A.; Zhou, Q. A. Exosomes—Nature's Lipid Nanoparticles, a Rising Star in Drug Delivery and Diagnostics. *ACS Nano* **2022**, *16*, 17802−17846.

(3) Fu, S.; Wang, Y.; Xia, X.; Zheng, J. C. Exosome Engineering: Current Progress in Cargo Loading and Targeted Delivery. *NanoImpact.* **2020**, *20*, 100261.

(4) Kimiz-Gebologlu, I.; Oncel, S. S. Exosomes: Large-Scale Production, Isolation, Drug Loading Efficiency, and Biodistribution and Uptake. *J. Controlled Release* **2022**, *347*, 533−543.

(5) Chen, H.; Wang, L.; Zeng, X.; Schwarz, H.; Nanda, H. S.; Peng, X.; Zhou, Y. Exosomes, a New Star for Targeted Delivery. *Frontiers in Cell and Developmental Biology.* **2021**, *9*, 751079.

(6) Shahabipour, F.; Barati, N.; Johnston, T. P.; Derosa, G.; Maffioli, P.; Sahebkar, A. Exosomes: Nanoparticulate Tools for RNA Interference and Drug Delivery. *J. Cell. Physiol.* **2017**, *232*, 1660−1668.

(7) Liu, C.; Su, C. Design Strategies and Application Progress of Therapeutic Exosomes. *Theranostics.* **2019**, *9*, 1015−1028.

(8) Xu, M., Yang, Q., Sun, X., Wang, Y. Recent Advancements in the Loading and Modification of Therapeutic Exosomes. *Frontiers in Bioengineering and Biotechnology* **2020**, *8*, DOI: 10.3389/fbioe.2020.586130.

(9) Wang, J.; Chen, D.; Ho, E. A. Challenges in the Development and Establishment of Exosome-Based Drug Delivery Systems. *J. Controlled Release* **2021**, *329*, 894−906.

(10) Morshedi Rad, D.; Alsadat Rad, M.; Razavi Bazaz, S.; Kashaninejad, N.; Jin, D.; Ebrahimi Warkiani, M. A Comprehensive Review on Intracellular Delivery. *Adv. Biomater. (Weinheim, Ger.).* **2021**, *33*, 2005363.

(11) Sensale, S.; Peng, Z.; Chang, H.-C. Acceleration of DNA Melting Kinetics Using Alternating Electric Fields. *Journal of Chemical Physics.* **2018**, *149*, No. 085102.

(12) Slouka, Z.; Senapati, S.; Chang, H.-C. Microfluidic Systems with Ion-Selective Membranes. *Annu. Rev. Anal. Chem.* **2014**, *7*, 317−335.

(13) Fuhrmann, G.; Serio, A.; Mazo, M.; Nair, R.; Stevens, M. M. Active Loading into Extracellular Vesicles Significantly Improves the Cellular Uptake and Photodynamic Effect of Porphyrins. *J. Controlled Release* **2015**, *205*, 35−44.

(14) Herrmann, I. K.; Wood, M. J. A.; Fuhrmann, G. Extracellular Vesicles As a Next-Generation Drug Delivery Platform. *Nat. Nanotechnol.* **2021**, *16*, 748−759.

(15) Rankin-Turner, S.; Vader, P.; O'Driscoll, L.; Giebel, B.; Heaney, L. M.; Davies, O. G. A Call for the Standardised Reporting of Factors Affecting the Exogenous Loading of Extracellular Vesicles with Therapeutic Cargos. *Adv. Drug Delivery Rev.* **2021**, *173*, 479−491.

(16) O'Loughlin, A. J.; Mäger, I.; de Jong, O. G.; Varela, M. A.; Schiffelers, R. M.; El Andaloussi, S.; Wood, M. J.; Vader, P. Functional Delivery of Lipid-Conjugated siRNA by Extracellular Vesicles. *Mol. Ther.* **2017**, *25*, 1580−1587.

(17) Pomatto, M. A.; Bussolati, B.; D'Antico, S.; Ghiotto, S.; Tetta, C.; Brizzi, M. F.; Camussi, G. Improved Loading of Plasma-Derived Extracellular Vesicles to Encapsulate Antitumor miRNAs. *Mol. Ther.–Methods Clin. Dev.* **2019**, *13*, 133−144.

(18) Haney, M. J.; Klyachko, N. L.; Zhao, Y.; Gupta, R.; Plotnikova, E. G.; He, Z.; Patel, T.; Piroyan, A.; Sokolsky, M.; Kabanov, A. V.; Batrakova, E. V. Exosomes As Drug Delivery Vehicles for Parkinson's Disease Therapy. *J. Controlled Release* **2015**, *207*, 18−30.
(19) Chen, P.; Yue, H.; Zhai, X.; Huang, Z.; Ma, G. H.; Wei, W.; Yan, L. T. Transport of a Graphene Nanosheet Sandwiched Inside Cell Membranes. *Sci. Adv.* **2019**, *5*, eaaw3192.
(20) Suzuki, N.; Wang, Y.; Elvati, P.; Qu, Z. B.; Kim, K.; Jiang, S.; Baumeister, E.; Lee, J.; Yeom, B.; Bahng, J. H.; Lee, J. Chiral Graphene Quantum Dots. *ACS Nano* **2016**, *10*, 1744−1755.
(21) Liu, C.; Elvati, P.; Majumder, S.; Wang, Y.; Liu, A. P.; Violi, A. Predicting the Time of Entry of Nanoparticles in Lipid Membranes. *ACS Nano* **2019**, *13*, 10221−10232.
(22) Yeom, J.; Guimaraes, P. P.; Ahn, H. M.; Jung, B. K.; Hu, Q.; McHugh, K.; Mitchell, M. J.; Yun, C. O.; Langer, R.; Jaklenec, A. Chiral Supraparticles for Controllable Nanomedicine. *Adv. Mater. (Weinheim, Ger.)*. **2020**, *32*, 1903878.
(23) Baimanov, D.; Wang, J.; Zhang, J.; Liu, K.; Cong, Y.; Shi, X.; Zhang, X.; Li, Y.; Li, X.; Qiao, R.; Zhao, Y. In Situ Analysis Of Nanoparticle Soft Corona and Dynamic Evolution. *Nat. Commun.* **2022**, *13*, 5389.
(24) Mitchell, M. J.; Billingsley, M. M.; Haley, R. M.; Wechsler, M. E.; Peppas, N. A.; Langer, R. Engineering precision nanoparticles for drug delivery. *Nat. Rev. Drug Discovery.* **2021**, *20*, 101−124.
(25) Yeom, J.; Guimaraes, P. P.; Ahn, H. M.; Jung, B. K.; Hu, Q.; McHugh, K.; Mitchell, M. J.; Yun, C. O.; Langer, R.; Jaklenec, A. Chiral Supraparticles for Controllable Nanomedicine. *Adv. Mater.* **2020**, *32*, e1903878.
(26) Chen, F.; Gao, W.; Qiu, X.; Zhang, H.; Liu, L.; Liao, P.; Fu, W.; Luo, Y. Graphene Quantum Dots in Biomedical Applications: Recent Advances and Future Challenges. *Frontiers in Laboratory Medicine.* **2017**, *1*, 192−199.
(27) Hai, X.; Feng, J.; Chen, X.; Wang, J. Tuning the Optical Properties of Graphene Quantum Dots for Biosensing and Bioimaging. *J. Mater. Chem. B* **2018**, *6*, 3219−3234.
(28) Tian, P.; Tang, L.; Teng, K. S.; Lau, S. P. Graphene Quantum Dots from Chemistry to Applications. *Mater. Today Chem.* **2018**, *10*, 221−258.
(29) Baimanov, D.; Wu, J.; Chu, R.; Cai, R.; Wang, B.; Cao, M.; Tao, Y.; Liu, J.; Guo, M.; Wang, J.; Yuan, X.; et al. Immunological Responses Induced by Blood Protein Coronas on Two-Dimensional MoS2 Nanosheets. *ACS Nano* **2020**, *14*, 5529−5542.
(30) Razmi, H.; Mohammad-Rezaei, R. Graphene Quantum Dots As a New Substrate for Immobilization and Direct Electrochemistry of Glucose Oxidase: Application to Sensitive Glucose Determination. *Biosens. Bioelectron.* **2013**, *41*, 498−504.
(31) Li, Z.; Fan, J.; Tong, C.; Zhou, H.; Wang, W.; Li, B.; Liu, B.; Wang, W. A Smart Drug-Delivery Nanosystem Based on Carboxylated Graphene Quantum Dots for Tumor-Targeted Chemotherapy. *Nanomedicine (London, U. K.)*. **2019**, *14*, 2011−2025.
(32) Ahmadi-Kashani, M.; Dehghani, H.; Zarrabi, A. A Biocompatible Nanoplatform Formed by Mgal-Layered Double Hydroxide Modified Mn3O4/N-Graphene Quantum Dot Conjugated-Polyaniline for Ph-Triggered Release of Doxorubicin. *Materials Science and Engineering: C* **2020**, *114*, 111055.
(33) Skotland, T.; Sandvig, K.; Llorente, A. Lipids in Exosomes: Current Knowledge and the Way Forward. *Prog. Lipid Res.* **2017**, *66*, 30−41.
(34) Abels, E. R.; Breakefield, X. O. Introduction to Extracellular Vesicles: Biogenesis, RNA Cargo Selection, Content, Release, and Uptake. *Cell. Mol. Neurobiol.* **2016**, *36*, 301−312.
(35) Li, G.; Luican, A.; Lopes dos Santos, J. M.; Castro Neto, A. H.; Reina, A.; Kong, J.; Andrei, E. Y. Observation of Van Hove Singularities in Twisted Graphene Layers. *Nat. Phys.* **2010**, *6*, 109−113.
(36) Zhang, S.; Song, A.; Chen, L.; Jiang, C.; Chen, C.; Gao, L.; Hou, Y.; Liu, L.; Ma, T.; Wang, H.; Feng, X. Q. Abnormal Conductivity in Low-Angle Twisted Bilayer Graphene. *Sci. Adv.* **2020**, *6*, eabc5555.
(37) Eriksson, M. O.; Schmidt, S.; Asghar, M.; Lin, P. C.; Holtz, P. O.; Syväjärvi, M.; Yazdi, G. R. Tuning the Emission Energy of Chemically Doped Graphene Quantum Dots. *Nanomaterials.* **2016**, *6*, 198.
(38) Jin, S. H.; Kim, D. H.; Jun, G. H.; Hong, S. H.; Jeon, S. Tuning the Photoluminescence of Graphene Quantum Dots through the Charge Transfer Effect of Functional Groups. *ACS Nano* **2013**, *7*, 1239−1245.
(39) Huang, B.; Bates, M.; Zhuang, X. Super-Resolution Fluorescence Microscopy. *Annu. Rev. Biochem.* **2009**, *78*, 993−1016.
(40) Aiello, C. D.; Abendroth, J. M.; Abbas, M.; Afanasev, A.; Agarwal, S.; Banerjee, A. S.; Beratan, D. N.; Belling, J. N.; Berche, B.; Botana, A.; Caram, J. R.; et al. A Chirality-Based Quantum Leap. *ACS Nano* **2022**, *16*, 4989−5035.
(41) Russ, K. A.; Elvati, P.; Parsonage, T. L.; Dews, A.; Jarvis, J. A.; Ray, M.; Schneider, B.; Smith, P. J.; Williamson, P. T.; Violi, A.; Philbert, M. A. C60 Fullerene Localization and Membrane Interactions in RAW 264.7 Immortalized Mouse Macrophages. *Nanoscale.* **2016**, *8*, 4134−4144.
(42) Guo, R.; Mao, J.; Yan, L.-T. Computer Simulation of Cell Entry of Graphene Nanosheet. *Biomaterials.* **2013**, *34*, 4296−4301.
(43) Dallavalle, M.; Calvaresi, M.; Bottoni, A.; Melle-Franco, M.; Zerbetto, F. Graphene Can Wreak Havoc with Cell Membranes. *ACS Appl. Mater. Interfaces.* **2015**, *7*, 4406−4414.
(44) Li, Y.; Wang, X.; Miao, J.; Li, J.; Zhu, X.; Chen, R.; Tang, Z.; Pan, R.; He, T.; Cheng, J. Chiral Transition Metal Oxides: Synthesis, Chiral Origins, and Perspectives. *Adv. Biomater. (Weinheim, Ger.)*. **2020**, *32*, 1905585.
(45) Vázquez-Nakagawa, M.; Rodríguez-Pérez, L.; Martín, N.; Herranz, MÁ. Supramolecular Assembly of Edge Functionalized Top-Down Chiral Graphene Quantum Dots. *Angew. Chem., Int. Ed.* **2022**, *61*, No. e202211365.
(46) Kuznetsova, V. A.; Mates-Torres, E.; Prochukhan, N.; Marcastel, M.; Purcell-Milton, F.; O'Brien, J.; Visheratina, A. K.; Martinez-Carmona, M.; Gromova, Y.; Garcia-Melchor, M.; Gun'ko, Y. K. Effect of Chiral Ligand Concentration and Binding Mode on Chiroptical Activity of CdSe/CdS Quantum Dots. *ACS Nano* **2019**, *13*, 13560−13572.
(47) Du, Y.-X.; Zhou, L.-J.; Guo, J.-G. The Influence of Strain Range, Size and Chiral on Mechanical Properties of Graphene: Molecular Dynamics Insights. *Nanomater. Nanotechnol.* **2022**, *12*, 18479804221110023.
(48) Monti, D.; Venanzi, M.; Stefanelli, M.; Sorrenti, A.; Mancini, G.; Di Natale, C.; Paolesse, R. Chiral Amplification of Chiral Porphyrin Derivatives by Templated Heteroaggregation. *J. Am. Chem. Soc.* **2007**, *129*, 6688−6689.
(49) Ghanbari, N.; Salehi, Z.; Khodadadi, A. A.; Shokrgozar, M. A.; Saboury, A. A.; Farzaneh, F. Tryptophan-Functionalized Graphene Quantum Dots with Enhanced Curcumin Loading Capacity and Ph-Sensitive Release. *J. Drug Delivery Sci. Technol.* **2021**, *61*, 102137.
(50) Eda, G.; Lin, Y. Y.; Mattevi, C.; Yamaguchi, H.; Chen, H. A.; Chen, I. S.; Chen, C. W.; Chhowalla, M. Blue Photoluminescence from Chemically Derived Graphene Oxide. *Adv. Biomater. (Weinheim, Ger.)*. **2010**, *22*, 505−509.
(51) Nguyen, M.-K.; Kuzyk, A. Reconfigurable Chiral Plasmonics beyond Single Chiral Centers. *ACS Nano* **2019**, *13*, 13615−13619.
(52) Yao, H.; Miki, K.; Nishida, N.; Sasaki, A.; Kimura, K. Large Optical Activity of Gold Nanocluster Enantiomers Induced by a Pair of Optically Active Penicillamines. *J. Am. Chem. Soc.* **2005**, *127*, 15536−15543.
(53) Ogawa, Y. Electron Microdiffraction Reveals the Nanoscale Twist Geometry of Cellulose Nanocrystals. *Nanoscale.* **2019**, *11*, 21767−21774.
(54) Wallbrecher, R.; Ackels, T.; Olea, R. A.; Klein, M. J.; Caillon, L.; Schiller, J.; Bovée-Geurts, P. H.; van Kuppevelt, T. H.; Ulrich, A. S.; Spehr, M.; Adjobo-Hermans, M. J. Membrane Permeation of Arginine-Rich Cell-Penetrating Peptides Independent of Transmembrane Potential As a Function of Lipid Composition and Membrane Fluidity. *J. Controlled Release* **2017**, *256*, 68−78.

https://doi.org/10.1021/acsnano.3c00305
ACS Nano XXXX, XXX, XXX−XXX

(55) Jang, S. C.; Kim, O. Y.; Yoon, C. M.; Choi, D. S.; Roh, T. Y.; Park, J.; Nilsson, J.; Lotvall, J.; Kim, Y. K.; Gho, Y. S. Bioinspired Exosome-Mimetic Nanovesicles for Targeted Delivery of Chemotherapeutics to Malignant Tumors. *ACS Nano* **2013**, *7*, 7698−7710.
(56) Hashemzadeh, H.; Raissi, H. Understanding Loading, Diffusion and Releasing of Doxorubicin and Paclitaxel Dual Delivery in Graphene and Graphene Oxide Carriers As Highly Efficient Drug Delivery Systems. *Appl. Surf. Sci.* **2020**, *500*, 144220.
(57) Sawy, A. M.; Barhoum, A.; Gaber, S. A.; El-Hallouty, S. M.; Shousha, W. G.; Maarouf, A. A.; Khalil, A. S. Insights of Doxorubicin Loaded Graphene Quantum Dots: Synthesis, DFT Drug Interactions, and Cytotoxicity. *Materials Science and Engineering: C* **2021**, *122*, 111921.
(58) Zhang, Y.; Chen, X.; Yuan, S.; Wang, L.; Guan, X. Joint Entropy-Assisted Graphene Oxide-Based Multiplexing Biosensing Platform for Simultaneous Detection of Multiple Proteases. *Anal. Chem.* **2020**, *92*, 15042−15049.
(59) Haney, M. J.; Zhao, Y.; Jin, Y. S.; Li, S. M.; Bago, J. R.; Klyachko, N. L.; Kabanov, A. V.; Batrakova, E. V. Macrophage-Derived Extracellular Vesicles as Drug Delivery Systems for Triple Negative Breast Cancer (TNBC) Therapy. *Journal of Neuroimmune Pharmacology.* **2020**, *15*, 487−500.
(60) Yamamoto, E.; Miyazaki, S.; Aoyama, C.; Kato, M. A Simple and Rapid Measurement Method of Encapsulation Efficiency of Doxorubicin Loaded Liposomes by Direct Injection of the Liposomal Suspension to Liquid Chromatography. *Int. J. Pharm.* **2018**, *536*, 21−28.
(61) Schindler, C.; Collinson, A.; Matthews, C.; Pointon, A.; Jenkinson, L.; Minter, R. R. Exosomal Delivery of Doxorubicin Enables Rapid Cell Entry and Enhanced In Vitro Potency. *PLoS One.* **2019**, *14*, No. e0214545.
(62) Teng, Y.; Yuan, S.; Shi, J.; Pong, P. W. T. A Multifunctional Nanoplatform Based on Graphene Quantum Dots-Cobalt Ferrite for Monitoring of Drug Delivery and Fluorescence/Magnetic Resonance Bimodal Cellular Imaging. *Adv. NanoBiomed Res.* **2022**, *2*, 2200044.
(63) Kanasty, R.; Dorkin, J. R.; Vegas, A.; Anderson, D. Delivery Materials for siRNA Therapeutics. *Nat. Mater.* **2013**, *12*, 967−977.
(64) Chan, M.-H.; Chang, Z.-X.; Huang, C-YF; Lee, L. J.; Liu, R.-S.; Hsiao, M. Integrated Therapy Platform of Exosomal System: Hybrid Inorganic/Organic Nanoparticles with Exosomes for Cancer Treatment. *Nanoscale Horiz.* **2022**, *7*, 352−367.
(65) Lu, M.; Zhao, X.; Xing, H.; Xun, Z.; Zhu, S.; Lang, L.; Yang, T.; Cai, C.; Wang, D.; Ding, P. Comparison of Exosome-Mimicking Liposomes with Conventional Liposomes for Intracellular Delivery of siRNA. *Int. J. Pharm.* **2018**, *550*, 100−113.
(66) Luan, X.; Sansanaphongpricha, K.; Myers, I.; Chen, H.; Yuan, H.; Sun, D. Engineering Exosomes As Refined Biological Nanoplatforms for Drug Delivery. *Acta Pharmacol. Sin.* **2017**, *38*, 754−763.
(67) Zhang, Y.; Liu, Y.; Liu, H.; Tang, W. H. Exosomes: Biogenesis, Biologic Function and Clinical Potential. *Cell Biosci.* **2019**, *9*, 19.
(68) Chen, H., Wang, L., Zeng, X., Schwarz, H., Nanda, H. S., Peng, X., Zhou, Y. Exosomes, a New Star for Targeted Delivery. *Frontiers in Cell and Developmental Biology* **2021**, *9*, DOI: 10.3389/fcell.2021.751079.
(69) Ling, K.; Jiang, H.; Li, Y.; Tao, X.; Qiu, C.; Li, F.-R. A Self-Assembling RNA Aptamer-Based Graphene Oxide Sensor for the Turn-On Detection of Theophylline in Serum. *Biosens. Bioelectron.* **2016**, *86*, 8−13.
(70) Li, Q.; Li, Y.; Gu, B.; Fang, L.; Zhou, P.; Bao, S.; Huang, L.; Dai, X. Akt Phosphorylates Wnt Coactivator and Chromatin Effector Pygo2 at Serine 48 to Antagonize Its Ubiquitin/Proteasome-mediated Degradation. *J. Biol. Chem.* **2015**, *290*, 21553−21567.
(71) Zhu, Y.; Zhao, Y.; Wen, J.; Liu, S.; Huang, T.; Hatial, I.; Peng, X.; Al Janabi, H.; Huang, G.; Mittlesteadt, J.; Cheng, M.; et al. Targeting the Chromatin Effector Pygo2 Promotes Cytotoxic T Cell Responses and Overcomes Immunotherapy Resistance in Prostate Cancer. *Sci. Immunol.* **2023**, *8*, eade4656.
(72) Lu, X.; Pan, X.; Wu, C. J.; Zhao, D.; Feng, S.; Zang, Y.; Lee, R.; Khadka, S.; Amin, S. B.; Jin, E. J.; Shang, X.; et al. An In Vivo Screen Identifies PYGO2 as a Driver for Metastatic Prostate Cancer. *Cancer Res.* **2018**, *78*, 3823−3833.
(73) Murphy, D. E.; de Jong, O. G.; Brouwer, M.; Wood, M. J.; Lavieu, G.; Schiffelers, R. M.; Vader, P. Extracellular Vesicle-Based Therapeutics: Natural Versus Engineered Targeting and Trafficking. *Exp. Mol. Med.* **2019**, *51*, 1−12.
(74) Cui, S.; Wang, Y.; Gong, Y.; Lin, X.; Zhao, Y.; Zhi, D.; Zhou, Q.; Zhang, S. Correlation of the Cytotoxic Effects of Cationic Lipids with Their Headgroups. *Toxicol. Res. (Cambridge, U. K.).* **2018**, *7*, 473−479.
(75) Harrington, C. A.; Winther, M.; Garred, M. M. Use of Bioanalyzer Electropherograms for Quality Control and Target Evaluation in Microarray Expression Profiling Studies of Ocular Tissues. *Journal of ocular biology.* **2009**, *2*, 243−249.
(76) Wang, C.; Sensale, S.; Pan, Z.; Senapati, S.; Chang, H.-C. Slowing Down DNA Translocation Through Solid-State Nanopores by Edge-Field Leakage. *Nat. Commun.* **2021**, *12*, 140.
(77) Zhang, C.; Huo, X.; Zhu, Y.; Higginbotham, J. N.; Cao, Z.; Lu, X.; Franklin, J. L.; Vickers, K. C.; Coffey, R. J.; Senapati, S.; Wang, C. Electrodeposited Magnetic Nanoporous Membrane for High-Yield and High-Throughput Immunocapture of Extracellular Vesicles and Lipoproteins. *Commun. Biol.* **2022**, *5*, 1358.
(78) Wang, C.; Senapati, S.; Chang, H.-C. Liquid Biopsy Technologies Based on Membrane Microfluidics: High-Yield Purification and Selective Quantification of Biomarkers in Nanocarriers. *Electrophoresis.* **2020**, *41*, 1878−1892.
(79) Zhang, Y.; Chen, X.; Roozbahani, G. M.; Guan, X. Graphene Oxide-Based Biosensing Platform for Rapid and Sensitive Detection of HIV-1 Protease. *Anal. Bioanal. Chem.* **2018**, *410*, 6177−6185.
(80) Zhang, Y.; Chen, X.; Roozbahani, G. M.; Guan, X. Rapid and Sensitive Detection of The Activity of ADAM17 Using a Graphene Oxide-Based Fluorescence Sensor. *Analyst.* **2019**, *144*, 1825−1830.
(81) Zhang, Y.; Chen, X.; Wang, C.; Roozbahani, G. M.; Chang, H.-C.; Guan, X. Chemically Functionalized Conical PET Nanopore for Protein Detection at the Single-Molecule Level. *Biosens. Bioelectron.* **2020**, *165*, 112289.
(82) Ma, X.; Guo, Q.; Xie, Y.; Ma, H. Green Chemistry for the Preparation of L-Cysteine Functionalized Silver Nanoflowers. *Chem. Phys. Lett.* **2016**, *652*, 148−151.
(83) Luo, J.; Cote, L. J.; Tung, V. C.; Tan, A. T.; Goins, P. E.; Wu, J.; Huang, J. Graphene Oxide Nanocolloids. *J. Am. Chem. Soc.* **2010**, *132*, 17667−17669.
(84) Kim, J.; Shamul, J. G.; Shah, S. R.; Shin, A.; Lee, B. J.; Quinones-Hinojosa, A.; Green, J. J. Verteporfin-Loaded Poly(ethylene glycol)-Poly(beta-amino ester)-Poly(ethylene glycol) Triblock Micelles for Cancer Therapy. *Biomacromolecules.* **2018**, *19*, 3361−3370.

https://doi.org/10.1021/acsnano.3c00305
ACS Nano XXXX, XXX, XXX−XXX